nature methods

Article

https://doi.org/10.1038/s41592-024-02292-9

DART.2: bidirectional synaptic pharmacology with thousandfold cellular specificity

Received: 30 December 2022

Accepted: 25 April 2024

Published online: 14 June 2024

Check for updates

Brenda C. Shields[1,6], Haidun Yan[1,2,6], Shaun S. X. Lim[1], Sasha C. V. Burwell[2], Celine M. Cammarata[2], Elizabeth A. Fleming[2], S. Aryana Yousefzadeh[3], Victoria Z. Goldenshtein[1], Elizabeth W. Kahuno[1], Purav P. Vagadia[4], Marie H. Loughran[5], Lei Zhiquan[4], Mark E. McDonnell[5], Miranda L. Scalabrino[2], Mishek Thapa[2], Tammy M. Hawley[2], Greg D. Field[1,2], Court Hull[2], Gary E. Schiltz[4], Lindsey L. Glickfeld[2], Allen B. Reitz[5] & Michael R. Tadross[1,2]

Precision pharmacology aims to manipulate specific cellular interactions within complex tissues. In this pursuit, we introduce DART.2 (drug acutely restricted by tethering), a second-generation cell-specific pharmacology technology. The core advance is optimized cellular specificity—up to 3,000-fold in 15 min—enabling the targeted delivery of even epileptogenic drugs without off-target effects. Additionally, we introduce brain-wide dosing methods as an alternative to local cannulation and tracer reagents for brain-wide dose quantification. We describe four pharmaceuticals—two that antagonize excitatory and inhibitory postsynaptic receptors, and two that allosterically potentiate these receptors. Their versatility is showcased across multiple mouse-brain regions, including cerebellum, striatum, visual cortex and retina. Finally, in the ventral tegmental area, we find that blocking inhibitory inputs to dopamine neurons accelerates locomotion, contrasting with previous optogenetic and pharmacological findings. Beyond enabling the bidirectional perturbation of chemical synapses, these reagents offer intersectional precision—between genetically defined postsynaptic cells and neurotransmitter-defined presynaptic partners.

Brain circuits are composed of interconnected neurons that exhibit an intriguing design asymmetry: each neuron releases a limited set of transmitters yet detects a much broader variety. Even considering corelease capabilities[1], the number of transmitters released by a neuron is dwarfed by the diversity of receptors expressed. This evolutionarily conserved asymmetry not only raises questions about the basis of biological intelligence, but also offers opportunities to develop synapse manipulation technologies.

Advances in chemical-synapse manipulation have focused on genetically encoded tools with exquisite presynaptic cell-type specificity[2]. Achieving postsynaptic specificity with this approach remains challenging. For instance, blocking GABA (γ-aminobutyric acid) release from a genetically defined presynaptic neuron (Fig. 1a) cannot discriminate among its diverse postsynaptic recipients, which all express the $GABA_AR$ (γ-aminobutyric acid receptor). This concern extends to glutamate, which is sensed by the universally expressed AMPAR (α-amino-3-hydroxy-5-methylisoxazole-4-propionic acid receptor).

In principle, postsynaptic interventions can exploit the neurochemical asymmetry to provide two forms of synapse specificity. In this configuration, postsynaptic cells are genetically defined (Fig. 1b), while

[1]Department of Biomedical Engineering, Duke University, Durham, NC, USA. [2]Department of Neurobiology, Duke University, Durham, NC, USA. [3]Department of Psychology and Neuroscience, Duke University, Durham, NC, USA. [4]Department of Chemistry, Northwestern University, Evanston, IL, USA. [5]Fox Chase Therapeutics Discovery, Inc., Doylestown, PA, USA. [6]These authors contributed equally: Brenda C. Shields, Haidun Yan.
e-mail: michael.tadross@duke.edu

https://doi.org/10.1038/s41592-024-02292-9

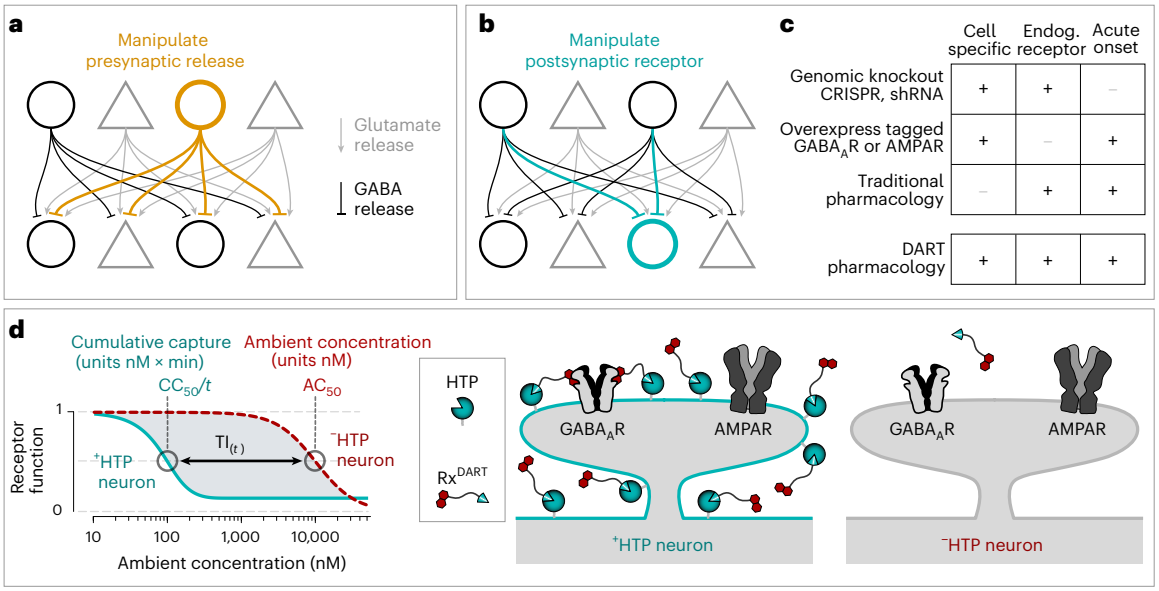

Fig. 1 | Overview of synapse manipulation tools. a, Presynaptic strategy. Manipulating presynaptic release from a genetically defined cell (orange cell) will affect all postsynaptic cells (triangular and circular cells express the $GABA_AR$). **b**, Postsynaptic strategy. Manipulating the $GABA_AR$ in a genetically defined neuron (cyan cell) alters its GABA inputs (cyan connections) without influencing GABA inputs to other cells (black connections). Glutamate signals are also preserved (gray connections). **c**, Technical challenges in implementing the postsynaptic strategy. Combining cell-type specificity, endogenous (Endog.)-receptor specificity and acute onset has been difficult. See Supplementary Discussion for details. **d**, Overview of DART. Dose–response relationship defines the key parameters AC_{50}, CC_{50} and $TI_{(t)}$. The example depicts a reagent with AC_{50} = 10,000 nM and CC_{50} = 5,000 nM × min after an incubation time of t = 50 min. The cartoon depicts an Rx^{DART}, which is a two-headed chemical consisting of a drug (Rx, red hexagons) linked to an HTL (cyan triangle). This HTL moiety is covalently captured by the HTP protein, which is expressed on cells of interest. Receptor specificity (for $GABA_AR$ versus AMPAR) and the type of manipulation (antagonism versus allosteric modulation) are inherited from the Rx.

additional precision would be achieved by leveraging receptor specificity. For instance, a cell-specific $GABA_AR$ antagonist would block GABA inputs to a given neuron while preserving its AMPAR-sensitivity to glutamate inputs. The approach would not alter how GABA is released or sensed by other cells.

Overall, the pre- versus postsynaptic strategies should be viewed as complementary, with neither supplanting the other. In the above examples, the presynaptic approach excels if one must differentiate between subtypes of GABA-releasing neurons (Fig. 1a). Conversely, the postsynaptic approach offers dual specificity between a genetically defined postsynaptic cell type and a transmitter-defined set of presynaptic cells (Fig. 1b).

In this work, we sought to create a toolkit for bidirectional manipulation of the AMPAR and $GABA_AR$ in genetically specified cells. To accomplish this, we leveraged DART (drug acutely restricted by tethering)[3], a technology that combines cell-type specificity, endogenous-receptor specificity and acute onset (Fig. 1c, refs. 3–13). The approach uses cell-type-specific expression of the HaloTag protein (HTP) in the desired postsynaptic cell type. This empowers the given cells to capture the HaloTag ligand (HTL) along with its covalently attached drug molecule (Rx), elevating the concentration of surface-tethered Rx to levels substantially higher than the ambient concentration. A crucial innovation in DART is that drugs are tethered to the cell surface rather than to the AMPAR or $GABA_AR$ themselves (Fig. 1c). The HTP does not interfere with mammalian signaling cascades, enabling its viral expression to define the cells of interest without altering their biology. Weeks later, one can deliver an Rx of choice, which specifies the receptor of interest (the endogenous $GABA_AR$ or AMPAR) and mode of action (antagonism or positive allosteric modulation).

We previously developed $YM90K^{DART}$, a cell-specific AMPAR antagonist, and demonstrated its use in behaving mice[3]. In particular, we discovered that cell-specific AMPAR antagonism in the striatum is therapeutic in a mouse model of Parkinson's disease. This was surprising as analogous manipulations lacking postsynaptic cellular specificity (for example, perturbation of presynaptic glutamate release and traditional AMPAR pharmacology in the striatum) exhibited little if any behavioral impact[14].

Nevertheless, technical challenges have limited the approach to pharmaceuticals with an overall suppressive effect on neural activity, for which brief ambient drug effects can clear without consequence. In contrast, because a $GABA_AR$ antagonist elevates neural activity, even brief ambient drug exposure can cause seizures with permanent damage. A related concern arises when dosing over large regions, including up to the whole brain, as a larger bolus of drug would exacerbate ambient effects at the site of infusion. Finally, allosteric modulation has yet to be demonstrated, as would be needed for boosting synaptic weights.

Here, DART.2 solves these challenges by providing three features. The first is improved cell specificity (up to 3,000-fold in 15 min), enabling safe delivery of an epileptogenic $GABA_AR$ antagonist in vivo. The second feature provides brain-wide pharmacology via a lateral-ventricular route of administration, paired with fluorescent tracers for whole-brain cellular target engagement. The third advance is extension to PAM (positive allosteric modulator) drugs for the $GABA_AR$ and AMPAR, enabling their bidirectional interrogation. We validate these tools across diverse brain regions and showcase conceptual utility by resolving contradictory findings from previous studies.

Results

Development of the DART.2 platform

An Rx^{DART} is a dual-functional chemical comprising an Rx and HTL connected by a flexible linker. Cellular specificity is governed by two key parameters: CC_{50} and AC_{50} (Fig. 1d). CC_{50} (cumulative capture 50%) specifies the concentration and exposure time (nM × min) needed for half-maximal tethered-drug effects on $^+$HTP cells (expressing functional HTP); this process is irreversible and driven by the HTL moiety. Conversely, AC_{50} (ambient concentration 50%) is the concentration

https://doi.org/10.1038/s41592-024-02292-9

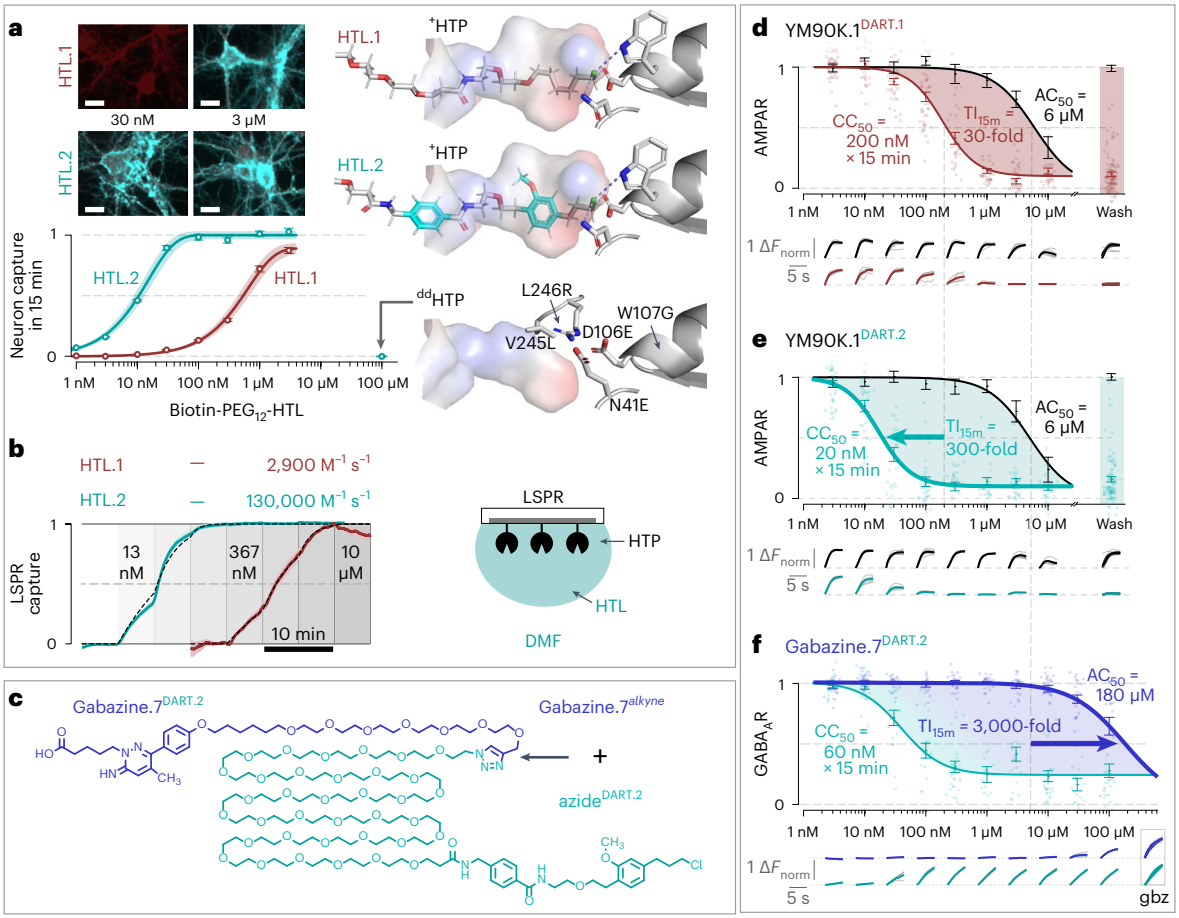

Fig. 2 | DART.2 achieves thousandfold cellular specificity. a, HTL.2 development. The top left shows a neuronal CC_{50} assay: $^{+}$HTP expression estimated via dTomato (dark red); captured biotin-PEG_{12}-HTL (post 15 min incubation) quantified with streptavidin (cyan). Scale bars, 10 µm. The bottom left shows dose–response data from 16 coverslips (8 concentrations × 2 ligands); the *y* axis shows normalized biotin-PEG_{12}-HTL capture (mean ± 95% CI from all neurons on one coverslip via regression-slope analysis). The right shows the structural model (Protein Data Bank (PDB) 4KAJ) of HTP with HTL.1 (top), HTL.2 (middle) and ^{dd}HTP mutations (bottom). **b**, Recombinant assay. Recombinant HTP immobilized on an LSPR sensor. HTL applied via digital micro-fluidics (DMF), 5 min per concentration (0 to 10 µM). LSPR traces (mean ± s.e.m., three technical replicates) and binding-model fit (dashed lines). **c**, Modular chemistry. Rx fragment (Rx–short spacer–alkyne) and HTL module (azide–long linker–HTL) assembled via alkyne–azide cycloaddition (for example, gabazine.7^{alkyne} + azide$^{DART.2}$ → gabazine.$7^{DART.2}$). **d**,**e**, AMPAR assay. ChR2-expressing neurons release glutamate onto cocultured neurons expressing GCaMP6s and $^{+}$HTP/^{dd}HTP. The top shows the population dose–response (error bars, mean ± s.e.m. over coverslips). The bottom shows single-neuron GCaMP6s waveforms. YM90K.$1^{DART.1}$, CC_{50} = 200 nM × 15 min ($^{+}$HTP 28 cells, n = 7 coverslips), AC_{50} = 6,000 nM (^{dd}HTP 144 cells, n = 8 coverslips), TI_{15m} = 30-fold (**d**) and YM90K.$1^{DART.2}$, CC_{50} = 20 nM × 15 min ($^{+}$HTP 27 cells, n = 8 coverslips), AC_{50} = 6,000 nM (^{dd}HTP 119 cells, n = 9 coverslips), TI_{15m} = 300-fold (**e**). **f**, $GABA_AR$ assay. ChR2, GCaMP6s and $^{+}$HTP/^{dd}HTP coexpressed in the same neuron, with excitatory synapses blocked. The top shows population dose–response (error bars, mean ± s.e.m. over cells). The bottom shows single-neuron GCaMP6s waveforms. 10 µM GABA is present throughout the assay. For gabazine.$7^{DART.2}$, CC_{50} = 60 nM × 15 min ($^{+}$HTP n = 18 cells) and AC_{50} = 180,000 nM (^{dd}HTP n = 21 cells), yielding TI_{15m} = 3,000-fold. gbz, traditional gabazine.

(nM) eliciting half-maximal drug effects on $^{-}$HTP cells (lacking HTP); this reversible equilibrium is set by the Rx moiety. The ratio AC_{50}/CC_{50} defines the therapeutic velocity, TV (in fold per min), which is multiplied by exposure time to obtain the therapeutic index, $TI_{(t)}$ (fold).

To enhance cellular specificity, our initial focus was to reduce the time and concentration needed for cumulative capture (that is, to minimize CC_{50}). Initial analyses revealed few stabilizing contacts between HTP and the original HTL.1 (Fig. 2a), indicating potential for shape and/or charge optimization. Using a synthon-based approach[15], we designed a series of HTL candidates that combine features from two structurally distinct ligands known to have affinity for exterior[16] and interior regions of HTP[17]. We focused on an aromatic ring substituent from each of these (Fig. 2a) and interconnected them with linkers of varying length, composition and points of attachment. We also explored sidechain diversity on the inner aromatic ring[17] (Supplementary Table 1).

We synthesized each HTL candidate, fused via a polyethylene glycol linker (PEG_{12}) to biotin, and tested capture efficiency on $^{+}$HTP neurons in culture (Extended Data Fig. 1a). After 15 min of incubation with ligand, cells were washed and surface biotin quantified (Fig. 2a). The best variant, named HTL.2, achieved CC_{50} = 10 nM × 15 min, 40 times better than HTL.1, with CC_{50} = 400 nM × 15 min. Subsequent surface plasmon resonance assays of recombinant HTP confirmed this finding, with HTL.2 exhibiting 45-fold accelerated binding compared to HTL.1 (Fig. 2b).

We standardized the design of Rx fragments and HTL modules for efficient coassembly via alkyne–azide click chemistry[18] (Fig. 2c and Supplementary Protocols). To accommodate the evolution of reagents, we introduced an expandable naming convention. Each fragment or module is named after its precursor, followed by a unique version number identifying conjugation and spacer details. To enhance clarity, given that many precursor names include numbers, we adopted the consistent use of a period to clearly separate the version number. This convention aims to improve readability and reduce confusion (Supplementary Discussion).

Finally, to improve rigor of control experiments, we developed an inactive HTP that cannot capture an Rx^{DART}, enabling measurement of ambient drug effects (AC_{50}) while controlling for effects of HTP expression. Initial attempts to mutate the D106 residue, to which HTL forms a covalent bond, led to either disrupted surface trafficking in neurons (for example, D106A) or residual capture (for example, D106E). We thus explored distributed mutations of the catalytic triad, combining D106E with W107G and N41E mutations. We further obstructed access to the catalytic site with bulky sidechains V245L and L246R (Fig. 2a), yielding a 'double dead' ^{dd}HTP, which retains neuronal surface trafficking while exhibiting zero measurable HTL.2 capture (Fig. 2a, 100 µM).

AMPAR and $GABA_AR$ antagonism with improved cell specificity

We synthesized an Rx fragment (YM90K.1^{alkyne}) and two HTL modules ($azide^{DART.1}$ and $azide^{DART.2}$). Following click-chemistry assembly, we obtained YM90K.$1^{DART.1}$ and YM90K.$1^{DART.2}$, which differ only in their HTL.1 versus HTL.2 moieties (Supplementary Table 2). In side-by-side neuronal assays of synaptic AMPAR signaling (Fig. 2d,e), both reagents exhibited similar off-target effects with an AC_{50} = 6 µM, as expected given their identical YM90K.1 moiety. In contrast, on-target effects differed considerably with YM90K.$1^{DART.1}$ requiring CC_{50} = 200 nM × 15 min (therapeutic index at 15 min, TI_{15m} = 30-fold), and improved YM90K.$1^{DART.2}$ with CC_{50} = 20 nM × 15 min (TI_{15m} = 300-fold).

We next focused on gabazine, a selective $GABA_AR$ antagonist. Given its epileptogenic nature, we anticipated that AC_{50} would be a critical parameter. We thus developed several variants, including gabazine.$1^{DART.2}$ (2-butyric acid, 5-H), gabazine.$5^{DART.2}$ (2-pentanoic acid, 5-H) and gabazine.$7^{DART.2}$ (2-pentanoic acid, 5-CH_3). Assaying endogenous $GABA_AR$s in primary neuronal culture (Fig. 2f) revealed that the most potent gabazine.$1^{DART.2}$ displays a TI_{15m} = 400-fold, the intermediate gabazine.$5^{DART.2}$ yields TI_{15m} = 1,700-fold and the attenuated gabazine.$7^{DART.2}$ achieves TI_{15m} = 3,000-fold, which is our maximum so far (Fig. 2f, Extended Data Fig. 2 and Supplementary Discussion).

In vivo $GABA_AR$ antagonism of cerebellar granule cells

In exploring $GABA_AR$ pharmacology in behaving mice, we focused on the input layer of the cerebellar cortex, which transforms glutamatergic mossy-fiber input onto a larger number of granule cells. This transformation, central to the Marr–Albus theory of cerebellar learning[19,20], is not fully understood, particularly regarding GABA's influence on granule cell activity[21]. While traditional presynaptic tools would inhibit GABA release onto all cells in the microcircuit, DART affects how granule cells respond to GABA, while preserving natural GABA release and its impact on neighboring cells (Fig. 3a).

To specifically target granule cells, we made adeno-associated virus (AAV) expression dependent on Cre recombinase and used BACα6Cre-C mice[22]. To adhere to the 4.7 kb packaging capacity of AAV, we replaced the transmembrane anchor from previous designs[3] with a shorter glycosylphosphatidylinositol (GPI) anchor, reducing the construct from 5.2 to 4.5 kb and enhancing AAV packaging (Extended Data Fig. 1c). We further selected an AAV_{7m8} serotype, which we found improved expression in this cell type. We validated potency and cellular specificity of these AAV-DIO-$^{+}HTP_{GPI}$ and AAV-DIO-$^{dd}HTP_{GPI}$ reagents in acute cerebellar slices, using whole-cell electrophysiology to measure tonic $GABA_AR$ current[23] (Fig. 3b). On $^{+}$HTP cells, gabazine.$1^{DART.2}$ antagonized $GABA_AR$ signaling at $CC_{50} \approx 20$ nM × 15 min, while off-target effects on ^{dd}HTP cells required AC_{50} of roughly 1,000 nM (Extended Data Fig. 3a).

To optically record neural activity, we used the same AAV reagents in BACα6Cre-C × Ai148 mice[24], which express genetically encoded calcium indicator (GCaMP6f) in granule cells, using an imaging window and cannula to visualize granule cell activity before and after drug delivery (Fig. 3c). Infusing gabazine.$1^{DART.2}$ in awake $^{+}$HTP mice caused a pronounced roughly ninefold increase in granule cell activity (Fig. 3c,d). The same infusion had no effect in ^{dd}HTP mice, indicating no measurable impact of the ambient compound (Fig. 3c). These findings not only validate the cell-type specificity of gabazine.$1^{DART.2}$, but also reveal a pronounced role of $GABA_ARs$ in modulating granule cell activity, supporting predictions of optimal signal-to-noise encoding[25]. In a companion study, we elaborate how such manipulations can elucidate population-level sensory information processing, advancing our understanding of Marr–Albus cerebellar learning[26].

An unexpected locomotor role for $GABA_AR \rightarrow VTA_{DA}$ signaling

Investigating GABA's influence on ventral tegmental area dopamine (VTA_{DA}) neurons, we observed that infusing gabazine.$1^{DART.2}$ into the VTA induced behavioral impairments in control mice, suggesting heightened sensitivity of this brain region to ambient drug. Consequently, we switched to the attenuated gabazine.$7^{DART.2}$ to minimize ambient effects. To validate efficacy, we performed VTA_{DA} neuron electrophysiology in acute midbrain slices prepared from DAT::Cre mice expressing either AAV-DIO-$^{+}HTP_{GPI}$ or AAV-DIO-$^{dd}HTP_{GPI}$. Gabazine.$7^{DART.2}$ potently blocked evoked $GABA_AR$ current onto $^{+}$HTP VTA_{DA} neurons without affecting ^{dd}HTP cells (Fig. 3e), underscoring its cell specificity. Additional tests confirmed that gabazine.$7^{DART.2}$, when tethered onto $^{+}$HTP cells, did not alter pacemaker firing rate or action potential waveform (Extended Data Fig. 3b,c), confirming receptor specificity for the $GABA_AR$.

We next looked for behavioral effects of the manipulation, using the same viral parameters along with an implanted cannula. Infusing gabazine.$7^{DART.2}$ had no impact on locomotion in ^{dd}HTP animals, nor any other observable behavioral effects. In contrast, the same infusion produced a significant increase in running speed in $^{+}$HTP mice, indicative of cell-specific potency (Fig. 3f). This locomotor effect persisted the next day, roughly 26 hours after the infusion, without an additional dose.

To substantiate our findings, we conducted two sets of analyses. First, in vivo pulse-chase experiments revealed that cell-surface HTP has a half-life of 1.5 ± 0.3 days (mean ± 95% confidence interval (CI) via nonlinear least squares fitting, Extended Data Fig. 3d,e). This turnover rate aligns with the persistent behavioral effects seen in our locomotor assay (Fig. 3f). Second, we undertook quantitative histology to scrutinize the influence of incidental spread to the neighboring substantia nigra pars compacta, home to canonical locomotor dopamine neurons. This analysis demonstrated no correlation between locomotor effects and incidental expression in the substantia nigra pars compacta (Extended Data Fig. 3f,g). Together, these data confirm that $GABA_A$ receptors on VTA_{DA} cells suppress locomotion (Fig. 3f), an unexpected insight elaborated in the discussion.

Quantitative cellular target engagement

In addition to answering key biological questions, a behavioral difference between manipulated and control animals often serves to establish technical validity. However, the absence of a behavioral effect casts doubt on technical validity. While histology can validate AAV expression, pharmaceutical interventions require further verification to confirm adequate ligand delivery in each subject.

Addressing this challenge, we developed $tracer^{DART.2}$ reagents, crafted to emulate an $Rx^{DART.2}$ in terms of diffusion and capture efficiency, but featuring a dye in lieu of the drug. We hypothesized that mixing these in a consistent one-to-ten ratio would allow each $tracer^{DART.2}$ molecule to serve as a visible proxy for ten $Rx^{DART.2}$ molecules nearby. Critically, for this ratiometric approach to be reliable, the mixed reagents must behave identically with regard to diffusion and capture.

We first examined whether DART reagents with different payloads diffuse equally in the brain. We synthesized physically diverse payloads amenable to fluorescence—Alexa488.$1^{DART.2}$ and Alexa647.$1^{DART.2}$ for direct visualization, and biotin.$1^{DART.2}$ as a smaller, non-fluorescent variant (Supplementary Table 2). When coinfused into mice expressing $^{+}HTP_{GPI}$, disparities in diffusion would manifest as varying fluorescence ratios with distance from the infusion site. In contrast, we

https://doi.org/10.1038/s41592-024-02292-9

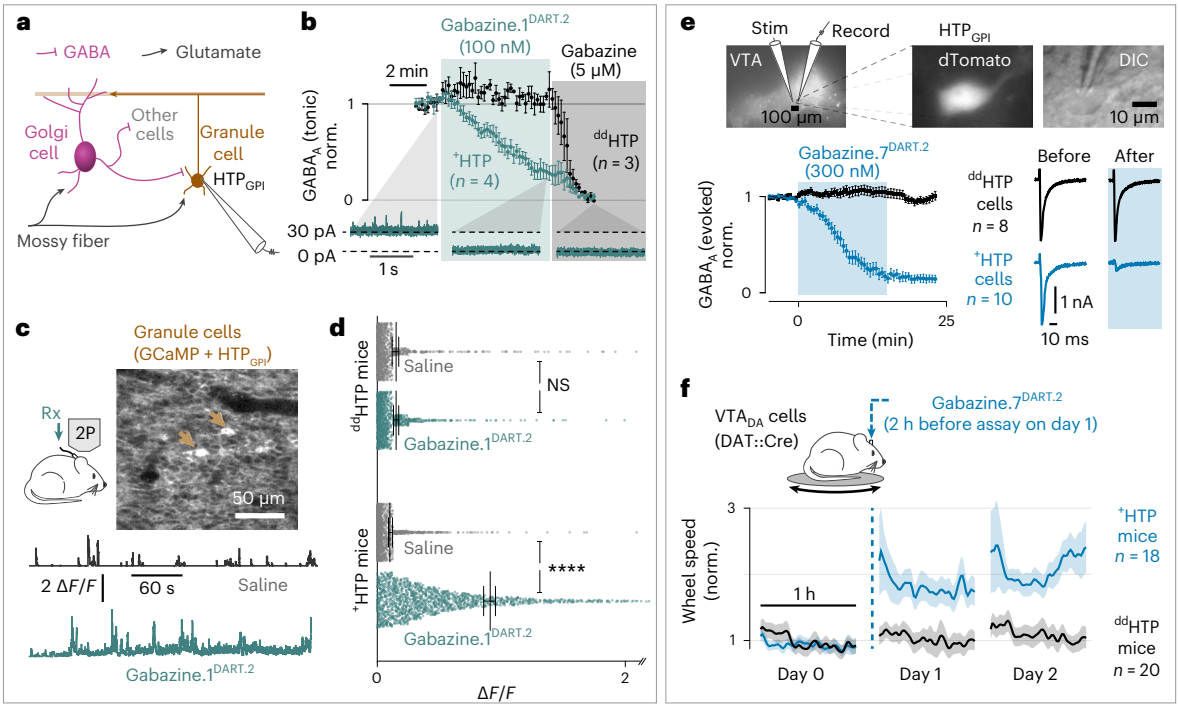

Fig. 3 | Safe delivery of epileptogenic drugs in behaving animals. a, Cerebellar circuit motivation. Gabazine.1$^{DART.2}$ exclusively antagonizes GABA$_A$Rs on granule cells without altering how GABA is released by Golgi cells. **b**, Cerebellar gabazine.1$^{DART.2}$ slice validation. Application of gabazine.1$^{DART.2}$ (100 nM). Top, data are mean ± s.e.m., cells normalized (norm.) to baseline. The bottom shows exemplar data from one cell. **c**, Cerebellar in vivo application. Top left shows a schematic of experimental setup. Baseline GCaMP6f granule cell recordings were succeeded by an infusion of 1 µl of ACSF with 1 µM gabazine.1$^{DART.2}$. After a 20 min interval, imaging was repeated (sensory stimuli absent throughout). The top right shows a representative field of view. The bottom shows example calcium traces (Δ*F*/*F*) in a $^{+}$HTP mouse before (saline) and after (1 µl of 1 µM gabazine.1$^{DART.2}$) infusion. **d**, Summary cerebellar in vivo data. Error bars indicate mean ± s.e.m. over cells. Each symbol represents one cell before (saline) and after (gabazine.1$^{DART.2}$) infusion. $^{+}$HTP cells exhibited a significant increase in GCaMP signals after gabazine.1$^{DART.2}$ (n = 1,707 cells from six mice, P = 0.0001, two-sided paired t-test), while ^{dd}HTP cells showed no significant change (n = 1,084 cells from four mice, P = 0.76, two-sided paired t-test). **e**, VTA gabazine.7$^{DART.2}$ slice validation. The top shows the evoked-IPSC configuration. The bottom shows 300 nM gabazine.7$^{DART.2}$ on ^{dd}HTP neurons versus $^{+}$HTP cells over assay duration ($^{+}$HTP = 86 ± 4% block). Data are mean ± s.e.m., cells normalized to baseline ($^{+}$HTP n = 10 cells; ^{dd}HTP n = 8 cells). Example traces to right. **f**, VTA in vivo application. Infusion of 1.2–1.8 µl of 10 µM gabazine.7$^{DART.2}$ into the VTA, locomotor speed in VTA$_{DA}$ $^{+}$HTP mice (blue trace, n = 18 mice) versus ^{dd}HTP control mice (black trace, n = 20 mice). Data were normalized to baseline speed. Solid line and shading are mean ± s.e.m. over mice ($P = 3 \times 10^{-5}$, two-sided unpaired t-test of $^{+}$HTP versus ^{dd}HTP mice, day 1–2 wheel-speed average). ****P < 0.0001; NS, not significant.

observed uniform pixel-wise correlations across the three color channels (Extended Data Fig. 4a–c), indicating equal diffusion.

Another pivotal requirement is equivalent capture efficiency across reagents, a characteristic not typically seen in commercial HaloTag reagents, for which capture is highly payload sensitive[27]. We scrutinized this assumption using a pulse-chase assay in cultured hippocampal neurons, first performing a dose–response with either an Alexa$^{DART.2}$ or various Rx$^{DART.2}$ reagents followed by a chase with biotin.1$^{DART.2}$ to label the remaining unbound HTP. This strategy revealed that CC_{50} is identical for all tested reagents (Extended Data Fig. 4d–h), affirming the equal-capture assumption.

We conducted behavioral experiments in the dorsal striatum, a key region for locomotion, to assess the effectiveness of the tracer$^{DART.2}$ strategy. Building on our previous work with YM90K$^{DART.1}$ delivery to Drd1a neurons in this brain region, we injected AAV-DIO-$^{+}$HTP$_{GPI}$ or AAV-DIO-^{dd}HTP$_{GPI}$ in Drd1a-Cre mice and implanted a cannula in the left dorsal striatum (Fig. 4a). We performed open-field behavior, both before and after infusion of a one-to-ten mixture of Alexa488.1$^{DART.2}$ + YM90K.1$^{DART.2}$ (3 µM dye + 30 µM drug, infusion: 1 µl in 10 min), quantifying turning via automated video tracking. Subsequent histological analysis measured dye capture in each animal (Fig. 4b), correlating it with behavioral data (Fig. 4c). Three key findings emerged. First, the turning bias seen only in $^{+}$HTP but not ^{dd}HTP mice confirms cell specificity of manipulation. Second, the tight correlation between behavioral effects and histological dye capture validates tracer$^{DART.2}$ as a reliable indicator of technical efficacy. Third, the exclusion of technical failures allowed for a more precise quantification of the behavioral effect (Fig. 4d), revealing it to be threefold larger than estimated in earlier studies[3].

Brain-wide dosing

We explored whether the improved capture kinetics of DART.2 could circumvent the need for cannulation directly into the investigated brain region. In preliminary experiments, we tested dosing via the cisterna magna, which showed rapid bio-distribution to the cortex[28]. However, we opted for lateral ventricle cannulation due to its more reliable stereotactic coordinates and mechanical stability. We characterized ambient pharmacokinetics in $^{-}$HTP mice by implanting a cannula in one ventricle and glass window over the contralateral visual cortex (Fig. 4e). Infusion of Alexa647.1$^{DART.2}$ into the ventricle produced an ambient fluorescence signal through the window, which peaked at roughly 2 hours and cleared by 24 hours (Extended Data Fig. 5a).

We targeted somatostatin interneurons (SOM cells) in the visual cortex using AAV-DIO-$^{+}$HTP$_{GPI}$ in SOM::Cre mice, along with pan-neuronal AAV-GCaMP8s to record activity in all cells. We presented oriented visual gratings to mice before and after infusion of 0.3 nM Alexa647.1$^{DART.2}$ + 3 nM YM90K.1$^{DART.2}$ (2 µl volume) into the contralateral ventricle. Alexa647.1$^{DART.2}$ accumulation was evident in the virus-expressing region (Fig. 4f). Animals with dense viral expression appeared to label $^{+}$HTP cells on the outer perimeter of expression before those in the center, suggesting ligand-limited dynamics. In animals with sparse expression, capture rose uniformly throughout

https://doi.org/10.1038/s41592-024-02292-9

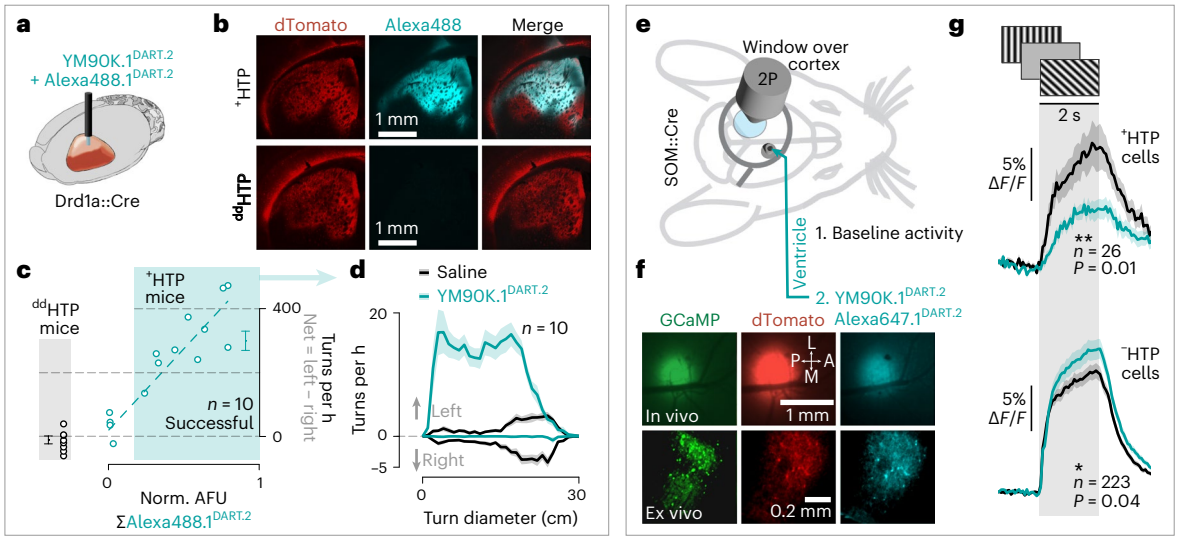

Fig. 4 | Quantitative target engagement and brain-wide dosing. a, Striatum experiment design. Mice with $^{+}$HTP or ^{dd}HTP in Drd1a cells of left dorsal striatum. Open field (1 h recording) was performed before and immediately after infusion of Alexa488.1$^{DART.2}$ + YM90K.1$^{DART.2}$ (3 µM dye + 30 µM drug, 1 µl in 10 min). **b**, Striatum histology. Histology performed 24 h after infusion, showing dTomato expression (red) and Alexa488.1$^{DART.2}$ capture (cyan) in one representative $^{+}$HTP mouse (top) and one representative ^{dd}HTP mouse (bottom). **c**, Striatum behavior versus histology correlation. Open-field turning versus dye capture relationship. Net turns (left turns minus right turns per hour) are graphed as a function of dye capture (integrated Alexa488.1^{DART}, arbitrary fluorescent units, AFU) for each $^{+}$HTP mouse (cyan symbols). Of 14 $^{+}$HTP mice, four were excluded for failed dye capture (cyan symbols outside the shading). Error bars are mean ± s.e.m. over the included mice (n = 10 $^{+}$HTP mice with successful dye capture; n = 8 ^{dd}HTP mice). **d**, Turn-diameter analysis. Histogram of turn diameter (1 cm bins) with left turns (upward histogram) tallied separately from right turns (downward histogram). Data are mean ± s.e.m. over the ten $^{+}$HTP mice that met histology inclusion criteria. Turn-diameter analysis was performed after saline infusion (black) and following Alexa488.1$^{DART.2}$ + YM90K.1$^{DART.2}$ infusion (cyan) in the same mice. **e**, Visual cortex experiment design. Mice expressing pan-neuronal GCaMP8s with SOM-specific $^{+}$HTP. Window over V1. Ligands delivered via the contralateral ventricle. **f**, Visual cortex histology. In vivo and ex vivo histology from one representative mouse. L, lateral; M, medial; P, posterior; A, anterior. **g**, Visual cortex neural activity. Mice presented oriented visual gratings, 2P Ca^{2+} imaging obtained before (black traces) and 5–6 h after (cyan traces) infusion of 0.3 nmol Alexa647.1$^{DART.2}$ + 3 nmol YM90K.1$^{DART.2}$ (2 µl volume) into the contralateral ventricle. Data show mean ± s.e.m. of cells from three mice. Following the manipulation, responses in $^{+}$HTP SOM cells is reduced (P = 0.01, n = 26, two-sided paired t-test) and responses in $^{-}$HTP, putative pyramidal cells increased (P = 0.04, n = 223, two-sided paired t-test). *P < 0.05; **P < 0.01.

the virus-expression region, suggesting an excess of ambient ligand, with capture plateauing after roughly 4 hours (Extended Data Fig. 5b). Given that CC_{50} = 300 nM × min for this reagent (Fig. 2e), we estimate that ambient levels in the cortex remained in the low nanomolar range (2.5 nM). Finally, we performed a pulse-chase experiment, which confirmed that a single bolus via the lateral ventricle suffices to saturate HTP in the cortex (Extended Data Fig. 5c,d).

Examining functional effects, $^{+}$HTP SOM cells displayed an attenuated response to visual gratings following drug delivery (Fig. 4g), consistent with antagonized sensitivity to glutamate excitation. Conversely, $^{-}$HTP cells, primarily pyramidal cells, exhibited a small but significant (P = 0.04, two-sided paired t-test) increase in response (Fig. 4g). This is consistent with the role of SOM cells in cortical inhibition, and thus disinhibition of adjacent cells. The impact of YM90K.1$^{DART.2}$ was most pronounced in cells with the highest baseline responsiveness (Extended Data Fig. 5e). Because YM90K.1$^{DART.2}$ alters glutamatergic inputs onto SOM cells without directly perturbing their voltage, it offers a distinction from previous research[29,30] and a topic for further exploration.

PAM design

Having developed competitive antagonists, our focus shifted to allosteric modulators. We started with the benzodiazepine site of the $GABA_AR$, which accommodates a spectrum of ligands ranging from negative allosteric modulation to PAM. We chose diazepam, a clinically relevant full-strength PAM, which adopts a $GABA_AR$ binding pose featuring a solvent-accessible amide[31]. We conjugated an alkyne to this amide and assembled diazepam.1$^{DART.2}$ using click chemistry (Supplementary Table 2). In our all-optical neuronal assay, diazepam.1$^{DART.2}$ showed excellent cellular specificity, with an AC_{50} = 38 µM on ^{dd}HTP neurons, CC_{50} = 50 nM × 15 min on $^{+}$HTP neurons and TI_{15m} = 760-fold. Critically, its maximum allosteric effect matched that of traditional diazepam (Extended Data Fig. 6a), indicating that the tether does not disrupt its conformational impact (Supplementary Discussion).

To complete the toolkit, we explored AMPAR PAMs, which modulate the receptor by binding to the dimeric interclamshell interface. Considering that most variants of this class (for example, cyclothiazide) require two drugs to bind in close proximity[32], we focused on newer scaffolds that bridge both sites. We chose CMPDA (phenyl-1,4-bisalkylsulfonamide) for its potent allosteric effects (stronger than cyclothiazide[33]) and available atomic structure. We synthesized CMPDA.1^{alkyne} using a short PEG spacer to span the distance from the binding site to free solution (Methods). While CMPDA.1^{alkyne} retained its ability to positively modulate the AMPAR, its function was lost on conversion to a full-length CMPDA.1^{DART} (Extended Data Fig. 6c). The reagent did not occlude other AMPAR PAMs, suggesting a lack of binding. Further structural analyses revealed a negative surface potential in the predicted path of the spacer, likely incompatible with our original electronegative PEG spacer design. We thus performed computational docking to design an electropositive amine-rich spacer, which we incorporated into CMPDA.2$^{DART.2}$. This design gained the ability to bind and produce positive allosteric modulation of the AMPAR (Extended Data Fig. 6d and Supplementary Discussion).

Bidirectional synaptic manipulations in the retina

We next explored bidirectional modulation of the AMPAR and $GABA_AR$ in a retina whole-mount preparation[34]. We used an established combination of viral serotype and mouse strain to express $^{+}HTP_{GPI}$ or $^{dd}HTP_{GPI}$ in parvalbumin-positive retinal ganglion cells (RGCs) (Fig. 5a). We then prepared whole-mount retina and measured evoked synaptic currents. Each recording established a stable baseline, followed by 15 min of

https://doi.org/10.1038/s41592-024-02292-9

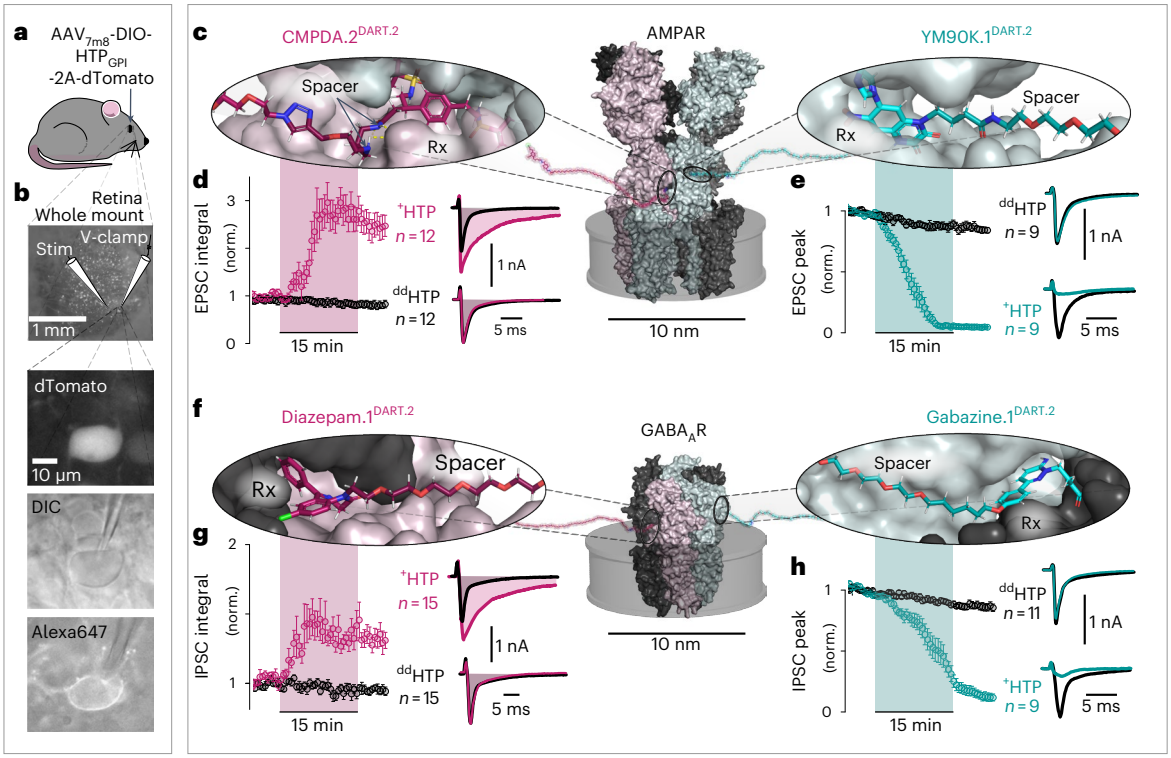

Fig. 5 | Bidirectional cell-specific AMPAR and $GABA_AR$ pharmacology. a, RGC expression strategy: intravitreal AAV_{7m8}-DIO-HTP_{GPI}-2A-dTomato in PV::cre mice. **b**, Whole retina preparation. Neurotransmission evoked (stim) and recorded (voltage-clamp) with conditions isolating AMPAR or $GABA_AR$. Following 15 min of 300 nM $Rx^{DART.2}$ + 30 nM Alexa647.1$^{DART.2}$, tethered dye envelopes $^{+}$HTP cell (one representative slice). **c**, AMPAR structural model. Cylinder depicts the cell membrane; structure is a composite of PDB 5WEO, 3RNN and 1FTL (PyMol rendering). The right shows that YM90K.1$^{DART.2}$ binds the orthosteric site. The left shows that CMPDA.2$^{DART.2}$ binds the interclamshell interface. **d**, CMPDA.2$^{DART.2}$ physiology. The right shows an example EPSC at baseline (gray) and after CMPDA.2$^{DART.2}$ (pink); shading depicts EPSC integral (nA × ms = pC). The left shows a time course of EPSC integral (baseline normalized; mean ± s.e.m. over cells), which reaches 2.6 ± 0.3 for $^{+}$HTP cells versus 0.9 ± 0.04 for ^{dd}HTP cells; $P = 1.6 \times 10^{-6}$ (two-sided unpaired *t*-test). **e**, YM90K.1$^{DART.2}$ physiology. The right shows an example EPSC at baseline (gray) and after YM90K.1$^{DART.2}$ (cyan). The left shows a time course of EPSC peak (baseline normalized; mean ± s.e.m. over cells), decreasing to 0.07 ± 0.02 for $^{+}$HTP cells versus 0.87 ± 0.03 for ^{dd}HTP cells; $P = 1.9 \times 10^{-13}$ (two-sided unpaired *t*-test). **f**, $GABA_AR$ structural model. Structure is a composite of PDB 6HUP and 6HUK (PyMol rendering). The left shows diazepam.1$^{DART.2}$ binds the α/δ interface. The right shows that gabazine.1$^{DART.2}$ binds the orthosteric α/β interface. **g**, Diazepam.1$^{DART.2}$ physiology. The right shows an example IPSC at baseline (gray) and following diazepam.1$^{DART.2}$ (pink); shading depicts IPSC integral (nA × ms = pC). The left shows the time course of IPSC integral (baseline normalized; mean ± s.e.m. over cells), which reaches 1.5 ± 0.1 for $^{+}$HTP cells versus 0.9 ± 0.04 for ^{dd}HTP cells; $P = 5.4 \times 10^{-6}$ (two-sided unpaired *t*-test). **h**, Gabazine.1$^{DART.2}$ physiology. The right shows an example IPSC at baseline (gray) and following gabazine.1$^{DART.2}$ (cyan). The left shows the time course of IPSC peak (baseline normalized; mean ± s.e.m. over cells), which drops to 0.26 ± 0.04 for $^{+}$HTP cells versus 0.89 ± 0.02 for ^{dd}HTP cells; $P = 1.7 \times 10^{-10}$ (two-sided unpaired *t*-test).

application of a given $Rx^{DART.2}$ (300 nM) + Alexa647.1$^{DART.2}$ (30 nM). Postexperiment imaging of Alexa647 confirmed ligand capture on $^{+}$HTP cells (Fig. 5b).

AMPAR reagents (Fig. 5c) were functionally characterized via evoked EPSC (excitatory postsynaptic current) recordings, with conditions isolating the AMPAR. CMPDA.2$^{DART.2}$ enhanced EPSCs in $^{+}$HTP RGCs, both by increasing peak amplitude and prolonging decay time (Extended Data Fig. 6f), culminating in a nearly threefold increase in integrated charge transfer relative to baseline (Fig. 5d). No impact of CMPDA.2$^{DART.2}$ was seen in analogous experiments in ^{dd}HTP RGCs (Fig. 5d). In samples expressing the same viral reagents, application of YM90K.1$^{DART.2}$ blocked the AMPAR-mediated EPSC exclusively in $^{+}$HTP RGCs with no impact on ^{dd}HTP cells (Fig. 5e).

The $GABA_AR$ toolset (Fig. 5f) was evaluated for its effects on $GABA_AR$-mediated IPSCs (inhibitory postsynaptic currents). Following diazepam.1$^{DART.2}$ application, IPSCs were potentiated on $^{+}$HTP RGCs: peak amplitude increased and decay time prolonged (Extended Data Fig. 6e), yielding an integrated charge transfer roughly 1.5 times the baseline (Fig. 5g). Finally, we confirmed that gabazine.1$^{DART.2}$ blocked the $GABA_AR$-mediated IPSC (Fig. 5h). Across all reagents, maximal effects took hold within 15 min in $^{+}$HTP RGCs, while no effects were seen on ^{dd}HTP RGCs.

Transcellular specificity of DART.2 pharmacology

Given that cellular membranes closely juxtapose in the brain, tethered drugs on the cell surface have the theoretical potential to act transcellularly. For instance, it remains unclear whether axon-tethered YM90K.1$^{DART.2}$ could act transcellularly to block the AMPAR. We previously proposed a theoretical model of the $^{+}$HTP membrane juxtaposed with a $^{-}$HTP membrane, separated by a synaptic cleft of varying height, h (Fig. 6a). This model predicts a steep decline in the tethered-drug concentration as a function of h, obeying a length constant of 1.8 nm, roughly an order of magnitude too short to span the synaptic cleft[3].

Given the importance of this question, we performed an empirical test of transcellular specificity. We favored a paired-patch configuration to maximize sensitivity, reasoning that transcellular effects might only become detectible in axons with high levels of $^{+}$HTP expression. In a subset of recordings, we observed reciprocal glutamatergic connections in both directions (Fig. 6b). Initial microscopy images depict the two neurons under dual-patch clamp, with the $^{+}$HTP neuron marked by a cytosolic dTomato and the ^{dd}HTP neuron identified via nuclear dTomato. Following Alexa647.1$^{DART.2}$ + YM90K.1$^{DART.2}$ incubation and washout, the $^{+}$HTP neuron is enveloped in dye, while the ^{dd}HTP neuron remains untouched (Fig. 6b).

https://doi.org/10.1038/s41592-024-02292-9

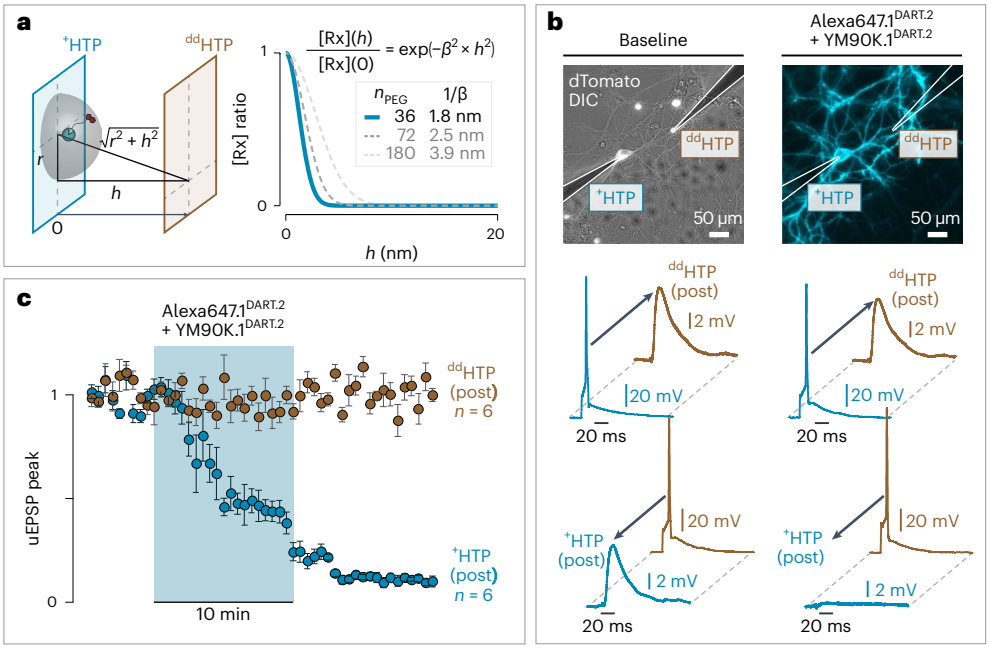

Fig. 6 | Transcellular specificity in DART.2 pharmacology. a, Theoretical tethered-drug distribution within synaptic cleft. We modeled an $^{+}$HTP membrane opposite a ^{dd}HTP membrane, separated by variable synaptic cleft height (h). **b**, Experimental verification of transcellular specificity. Representative data from one reciprocally connected pair of patch-clamped neurons. Cells are identified as $^{+}$HTP (cytosolic dTomato marker) and ^{dd}HTP (nuclear dTomato marker), shown before (left) and after (right) delivery of a 1:10 mixture of Alexa647.1$^{DART.2}$ + YM90K.1$^{DART.2}$. Postdelivery, the $^{+}$HTP neuron is enveloped in dye across all cellular compartments, in contrast to the dye-free ^{dd}HTP neuron (top row). Electrophysiological data demonstrate that synaptic transmission from the $^{+}$HTP to ^{dd}HTP neuron remains unimpeded postdelivery (middle row), while reciprocal transmission from the ^{dd}HTP to $^{+}$HTP neuron is abolished (bottom row). **c**, Summary data. Data are mean ± s.e.m. over independent paired-patch recordings, normalized to baseline unitary excitatory postsynaptic potential (uEPSP) peak amplitude. Synaptic transmission from ^{dd}HTP to $^{+}$HTP neurons following drug application (blue data) versus transmission in the reverse direction, from $^{+}$HTP to ^{dd}HTP neurons (brown data). High levels of presynaptic $^{+}$HTP dye capture were confirmed in all replicates.

Complementing these visual observations, our electrophysiological data reveal that synaptic transmission from this $^{+}$HTP neuron to the ^{dd}HTP counterpart remains intact after drug delivery (Fig. 6b). By contrast, for the same pair of neurons, synaptic transmission from ^{dd}HTP to $^{+}$HTP was entirely abolished (Fig. 6b). The latter finding confirms high levels of $^{+}$HTP expression on this specific neuron, thereby solidifying the former finding that axon-tethered drugs do not act transcellularly. The results are corroborated over several replicates (Fig. 6c), for which we confirmed high levels of presynaptic $^{+}$HTP dye capture. These findings support predictions of the tethered-diffusion model (Fig. 6a), and underscore the remarkable cell-specific action of DART.2 over nanoscale dimensions.

Discussion

In the rapidly advancing field of causal neuroscience, established methods typically manipulate action potentials or neurotransmitter release capabilities of genetically defined neurons. In this study, we introduce an approach that shifts the focus from neuronal output to the synaptic inputs received by a given neuron.

To underscore the capabilities of the approach, consider our study of GABA in the VTA. Previous studies, manipulating GABA secretion in the VTA or using local infusions of $GABA_AR$ pharmaceuticals, offered an incomplete view due to GABA's broad action on diverse VTA cell types. These studies suggest that, when activated collectively, $GABA_ARs$ in the VTA accelerate locomotion[35,36]. Our work diverges markedly from this narrative. By narrowing the focus to VTA_{DA} cells, we reveal that $GABA_ARs$ on these cells function not as a 'gas pedal' but rather as a locomotor 'brake'. This finding is especially striking when juxtaposed with past studies, wherein direct optogenetic stimulation of VTA_{DA} neurons did not overtly alter locomotion[37]. At first glance, this might seem discordant, as optogenetic excitation and $GABA_AR$ antagonism should both increase VTA_{DA} neuron activity. However, a deeper appreciation of VTA_{DA} dynamics offers reconciliation. For instance, widefield optogenetic stimulation would likely cause VTA_{DA} neurons to exhibit synchronous burst-firing[38,39]. In contrast, $GABA_AR$ antagonism on these cells may prevent the occurrence of synaptically mediated pauses, which are known to be heterogeneous across the VTA_{DA} population[40]. In emphasizing these distinctions one can begin to appreciate the complementary nature of these tools, which cannot readily substitute for one another.

Regarding technical insights, we were surprised that ambient effects of gabazine could be so severely attenuated (a 15-fold increase in AC_{50}) without major tradeoffs in tethered effects (a twofold increase in CC_{50}, while maintaining 75% max efficacy). Although initially unexpected, the findings are in quantitative agreement with a model of tethered diffusion, which offers insights into the development of future reagents (Extended Data Fig. 2 and Supplementary Discussion).

We recognize the importance of addressing prevalent questions and uncertainties, particularly those pertaining to DART's apparent divergence from conventional pharmacology principles. One prevalent query involves the role of ambient drug concentration, which is a critical parameter that must be carefully optimized in a standard pharmacological study. By contrast, the precise ambient concentration of an Rx^{DART} is not critical at low concentrations (well below AC_{50}). In this regime, ambient concentration only determines how long it takes to reach saturation, while the ultimate strength of the manipulation becomes solely determined by the level of $^{+}$HTP protein expression. Given these considerations, optimization of in vivo dosing requires only that saturation is achieved in $^{+}$HTP animals at a dose that is safe in control mice. Once dosing is determined for a given $Rx^{DART.2}$, one can rely on the identical diffusion and capture characteristics of the reagents to expedite dosing-optimization for other $Rx^{DART.2}$ ligands.

These properties have additional benefits with regard to slice experiments and their interpretability in comparison to in vivo work. First, DART.2 allows researchers to streamline slice experiments by focusing on a single dose, typically 300 nM, which reliably achieves $^{+}$HTP saturation in under 15 min. The focus can then shift toward characterizing the impact of the tethered drug. Moreover, by maintaining a consistent one-to-ten ratio of a given tracer$^{DART.2}$, one can leverage fluorescence as a metric of equivalence across experiments. Thus, in a divergence from traditional pharmacology, tracer$^{DART.2}$ can establish a quantitative comparison between drug-tethering to $^{+}$HTP cells in vivo and ex vivo, regardless of the ambient concentration.

Finally, it is important to note remaining limitations of the tool, which we hope to address in future iterations. Foremost among these is the challenge inherent in systemic delivery across the blood–brain barrier, particularly given that a PEG_{36} linker is unlikely to traverse cellular membranes. To this end, certain modifications to the PEG_{36} linker may promote blood–brain-barrier crossing[41], while branched ligands[42] could improve stoichiometry by delivering multiple drugs per molecule. Another desired feature is reversibility: photo-controlled versions of DART are possible[43,44] and are of interest for millisecond precision over optically accessible brain volumes. Conversely, light-independent reversibility would simplify use over greater brain volumes. With regard to subcellular precision, appending trafficking motifs to the genetic element could restrict drug delivery to the axon, soma or distal dendrite, which would be of interest given preferential innervation of these locales by distinct GABA-releasing cell types[45]. For finer-scale precision, an intersectional protein-based switch may one day target drugs to the synaptic contact between genetically defined pre- and postsynaptic neurons[46]. Finally, the method can be extended to pharmaceuticals that modulate a broader set of ionotropic receptors, metabotropic receptors and ion channels. In sum, the technologies described herein—and the conceptual questions now within reach—represent exciting areas of untapped promise.

Online content

Any methods, additional references, Nature Portfolio reporting summaries, source data, extended data, supplementary information, acknowledgements, peer review information; details of author contributions and competing interests; and statements of data and code availability are available at https://doi.org/10.1038/s41592-024-02292-9.

References

1. Tritsch, N. X., Granger, A. J. & Sabatini, B. L. Mechanisms and functions of GABA co-release. *Nat. Rev. Neurosci.* **17**, 139–145 (2016).
2. Rost, B. R., Wietek, J., Yizhar, O. & Schmitz, D. Optogenetics at the presynapse. *Nat. Neurosci.* **25**, 984–998 (2022).
3. Shields, B. C. et al. Deconstructing behavioral neuropharmacology with cellular specificity. *Science* **356**, eaaj2161 (2017).
4. Bailey, K. R., Rustay, N. R. & Crawley, J. N. Behavioral phenotyping of transgenic and knockout mice: practical concerns and potential pitfalls. *ILAR J.* **47**, 124–131 (2006).
5. Verma, R., Mohl, D. & Deshaies, R. J. Harnessing the power of proteolysis for targeted protein inactivation. *Mol. Cell* **77**, 446–460 (2020).
6. Gross, G. G. et al. An E3-ligase-based method for ablating inhibitory synapses. *Nat. Methods* **13**, 673–678 (2016).
7. Hayashi-Takagi, A. et al. Labelling and optical erasure of synaptic memory traces in the motor cortex. *Nature* **525**, 333–338 (2015).
8. Banghart, M., Borges, K., Isacoff, E., Trauner, D. & Kramer, R. H. Light-activated ion channels for remote control of neuronal firing. *Nat. Neurosci.* **7**, 1381–1386 (2004).
9. Volgraf, M. et al. Allosteric control of an ionotropic glutamate receptor with an optical switch. *Nat. Chem. Biol.* **2**, 47–52 (2006).
10. Broichhagen, J. & Levitz, J. Advances in tethered photopharmacology for precise optical control of signaling proteins. *Curr. Opin. Pharmacol.* **63**, 102196 (2022).
11. Szobota, S. et al. Remote control of neuronal activity with a light-gated glutamate receptor. *Neuron* **54**, 535–545 (2007).
12. Wyart, C. et al. Optogenetic dissection of a behavioural module in the vertebrate spinal cord. *Nature* **461**, 407–410 (2009).
13. Lin, W. C. et al. A comprehensive optogenetic pharmacology toolkit for in vivo control of GABA(A) receptors and synaptic inhibition. *Neuron* **88**, 879–891 (2015).
14. Gardoni, F. & Di Luca, M. Targeting glutamatergic synapses in Parkinson's disease. *Curr. Opin. Pharmacol.* **20**, 24–28 (2015).
15. Sadybekov, A. A. et al. Synthon-based ligand discovery in virtual libraries of over 11 billion compounds. *Nature* **601**, 452–459 (2022).
16. Los, G. V. et al. HaloTag: a novel protein labeling technology for cell imaging and protein analysis. *ACS Chem. Biol.* **3**, 373–382 (2008).
17. Neklesa, T. K. et al. A bidirectional system for the dynamic small molecule control of intracellular fusion proteins. *ACS Chem. Biol.* **8**, 2293–2300 (2013).
18. Rostovtsev, V. V., Green, L. G., Fokin, V. V. & Sharpless, K. B. A stepwise huisgen cycloaddition process: copper(I)-catalyzed regioselective 'ligation' of azides and terminal alkynes. *Angew. Chem. Int. Ed. Engl.* **41**, 2596–2599 (2002).
19. Marr, D. A theory of cerebellar cortex. *J. Physiol.* **202**, 437–470 (1969).
20. Albus, J. S. A theory of cerebellar function. *Math. Biosci.* **10**, 25–61 (1971).
21. Eccles, J. C., Llinas, R. & Sasaki, K. The mossy fibre-granule cell relay of the cerebellum and its inhibitory control by Golgi cells. *Exp. Brain Res.* **1**, 82–101 (1966).
22. Aller, M. I. et al. Cerebellar granule cell Cre recombinase expression. *Genesis* **36**, 97–103 (2003).
23. Brickley, S. G., Cull-Candy, S. G. & Farrant, M. Development of a tonic form of synaptic inhibition in rat cerebellar granule cells resulting from persistent activation of GABAA receptors. *J. Physiol.* **497**, 753–759 (1996).
24. Chen, T. W. et al. Ultrasensitive fluorescent proteins for imaging neuronal activity. *Nature* **499**, 295–300 (2013).
25. Duguid, I., Branco, T., London, M., Chadderton, P. & Hausser, M. Tonic inhibition enhances fidelity of sensory information transmission in the cerebellar cortex. *J. Neurosci.* **32**, 11132–11143 (2012).
26. Fleming, E. A., Field, G. D., Tadross, M. R. & Hull, C. Local synaptic inhibition mediates cerebellar granule cell pattern separation and enables learned sensorimotor associations. *Nat. Neurosci.* **27**, 689–701 (2024).
27. Wilhelm, J. et al. Kinetic and structural characterization of the self-labeling protein tags HaloTag7, SNAP-tag, and CLIP-tag. *Biochemistry* **60**, 2560–2575 (2021).
28. Iliff, J. J. et al. A paravascular pathway facilitates CSF flow through the brain parenchyma and the clearance of interstitial solutes, including amyloid β. *Sci. Transl. Med.* **4**, 147ra111 (2012).
29. Adesnik, H. Synaptic mechanisms of feature coding in the visual cortex of awake mice. *Neuron* **95**, 1147–1159 e1144 (2017).
30. Lee, S. H. et al. Activation of specific interneurons improves V1 feature selectivity and visual perception. *Nature* **488**, 379–383 (2012).
31. Masiulis, S. et al. GABAA receptor signalling mechanisms revealed by structural pharmacology. *Nature* **565**, 454–459 (2019).
32. Sun, Y. et al. Mechanism of glutamate receptor desensitization. *Nature* **417**, 245–253 (2002).

33. Timm, D. E., Benveniste, M., Weeks, A. M., Nisenbaum, E. S. & Partin, K. M. Structural and functional analysis of two new positive allosteric modulators of GluA2 desensitization and deactivation. *Mol. Pharmacol.* **80**, 267–280 (2011).
34. Masland, R. H. & Raviola, E. Confronting complexity: strategies for understanding the microcircuitry of the retina. *Annu. Rev. Neurosci.* **23**, 249–284 (2000).
35. Arnt, J. & Scheel-Kruger, J. GABA in the ventral tegmental area: differential regional effects on locomotion, aggression and food intake after microinjection of GABA agonists and antagonists. *Life Sci.* **25**, 1351–1360 (1979).
36. Tanner, T. GABA-induced locomotor activity in the rat, after bilateral injection into the ventral tegmental area. *Neuropharmacology* **18**, 441–446 (1979).
37. Tye, K. M. et al. Dopamine neurons modulate neural encoding and expression of depression-related behaviour. *Nature* **493**, 537–541 (2013).
38. Pan, W.-X., Coddington, L. T. & Dudman, J. T. Dissociable contributions of phasic dopamine activity to reward and prediction. *Cell Rep.* **36**, 109684 (2021).
39. Bolkan, S. S. et al. Opponent control of behavior by dorsomedial striatal pathways depends on task demands and internal state. *Nat. Neurosci.* **25**, 345–357 (2022).
40. Morikawa, H. & Paladini, C. A. Dynamic regulation of midbrain dopamine neuron activity: intrinsic, synaptic, and plasticity mechanisms. *Neuroscience* **198**, 95–111 (2011).
41. Pardridge, W. M. Delivery of biologics across the blood-brain barrier with molecular Trojan Horse technology. *BioDrugs* **31**, 503–519 (2017).
42. Acosta-Ruiz, A. et al. Branched photoswitchable tethered ligands enable ultra-efficient optical control and detection of G protein-coupled receptors in vivo. *Neuron* **105**, 446–463 e413 (2020).
43. Donthamsetti, P. et al. Cell specific photoswitchable agonist for reversible control of endogenous dopamine receptors. *Nat. Commun.* **12**, 4775 (2021).
44. Donthamsetti, P. C. et al. Genetically targeted optical control of an endogenous G protein-coupled receptor. *J. Am. Chem. Soc.* **141**, 11522–11530 (2019).
45. Veres, J. M., Nagy, G. A. & Hajos, N. Perisomatic GABAergic synapses of basket cells effectively control principal neuron activity in amygdala networks. *eLife* https://doi.org/10.7554/eLife.20721 (2017).
46. Kim, J. et al. mGRASP enables mapping mammalian synaptic connectivity with light microscopy. *Nat. Methods* **9**, 96–102 (2012).

Methods

Experimental model and subject details

All animal experiments were approved by the Duke Institutional Animal Care and Use Committee, an Association for Assessment and Accreditation of Laboratory Animal Care accredited program registered with the United States Department of Agriculture Public Health Service and the National Institutes of Health (NIH) Office of Animal Welfare Assurance, and conform to all relevant regulatory standards (Tadross protocols A160-17-06, A113-20-05 and A091-23-04).

Rats

Timed-pregnant female Sprague–Dawley rats (Charles River) were individually housed in a standard temperature (20.5–25.5 °C (69 °F minimum–78 °F maximum)) and humidity (30–70% minimum–maximum) environment, under a normal 12-h light–dark cycle and with food and water ad libitum.

Mice

Drd1a-Cre (GENSAT EY262, striatum D1 medium spiny neuron), DAT-*Ires*-cre (Jackson Laboratories, cat. no. 006660, VTA dopamine neuron), SST-Cre (Jackson Laboratories, cat. no. 013044, V1 SOM interneuron), PV-Cre (Jackson Laboratories, cat. no. 017320, RGC), BACα6Cre-A (Hatten Laboratory, Rockefeller, cerebellar granule cell) and Ai148D (Jackson Laboratories, cat. no. 030328, GCamp6f). Mice were group housed by age and gender (maximum of five per cage) in a standard temperature (20.5–25.5 °C (69 °F minimum–78 °F maximum)) and humidity (30–70% minimum–maximum) environment, under a normal 12-h light–dark cycle and with food and water provided ad libitum.

Quantification and statistical analysis

Reported values are mean ± s.e.m. Statistical tests were performed via Student's *t*-test (paired or unpaired), or nonlinear regression (MATLAB 2018b curve fitting toolbox). The statistical test, sample size and *P* value are indicated in each figure legend. No statistical methods were used to predetermine sample size. All experiments involving a quantitative comparison of an experimental parameter were performed in a manner to counterbalance uncontrolled sources of variability. In cultured neurons, data obtained to compare two or more reagents (for example, YM90K.1$^{DART.1}$ versus YM90K.1$^{DART.2}$) was obtained with experimental groups tested side by side, such that all comparison groups were equally represented in each batch of cells. For slice, retina and mouse behavior, positive versus negative groups (for example, HTP^{+} versus ^{dd}HTP mice) were interleaved and run side by side, using cage mates when possible, and balancing groups to minimize confounding differences (for example, animal sex, experimenter, time of year), with the goal of isolating the experimental variable of interest.

Chemical synthesis

See Supplementary Protocols for further details of chemical synthesis.

Genetic construct design

Genetic elements were concatenated via PCR, restriction digest, ligation and sequence verification, as follows:

- aavCAG-DIO-$^{+}$HTP$_{GPI}$-2A-dTomato-WPRE. Coding, SS$_{nlg}$-$^{+}$HTP-(GGSGG)$_8$-Thy1$_{GPI}$-2A-dTomato. SS$_{nlg}$, the signal peptide (residues 1–49) of mouse neuroligin-1; $^{+}$HTP, optimized variant of the HTP[16]; (GGSGG)8, linker with eight repeats of gly-gly-ser-gly-gly; Thy1$_{GPI}$ from Addgene_163696. Marker of Expression, 2A-dTomato, P2A ribosomal skip sequence and dTomato. Backbone, aavCAG-DIO-WPRE vector is from Addgene_100842.
- aavCAG-DIO-^{dd}HTP$_{GPI}$-2A-dTomato-WPRE. Coding, SS$_{nlg}$-^{dd}HTP-(GGSGG)$_8$-Thy1$_{GPI}$-2A-dTomato. ^{dd}HTP is the HTP with N41E, D106E, W107G, V245L and L246R mutations. Other elements as above.
- aavCAG-DIO-$^{+}$HTP$_{GPI}$-IRES-dTomatoF-W3SL. Coding, SS$_{nlg}$-$^{+}$HTP-(GGSGG)$_8$-Thy1$_{GPI}$-IRES-dTomatoF. IRES is the internal ribosomal entry site. dTomatoF is dTomato followed by the Farnesylation sequence KLNPPDESGPGCMSCKCVLS. W3SL is from Addgene_61463. Other elements as above.
- aavCAG-DIO-^{dd}HTP$_{GPI}$-IRES-dTomatoF-W3SL. Coding, SS$_{nlg}$-^{dd}HTP-(GGSGG)$_8$-Thy1$_{GPI}$-IRES-dTomato. Elements all as above.
- aavSYN-ChR2-HA-dsfGFP-WPRE. Coding, ChR2(H134R)-HA-dsfGFP. ChR2(H134R) is the optogenetic channelrhodopsin2; dsfGFP is superfolder green fluorescent protein (GFP) with T65G and Y66G mutations to eliminate fluorescence. Backbone, aavSYN-WPRE vector is from Addgene_100843.
- aavCAG-$^{+}$HTP$_{NLG(432-648)ERXL}$-2A-dTomato-WPRE. Coding, SS$_{nlg}$-HA-$^{+}$HTP- NLG(432-648)-ERXL. HA, the hemagglutinin epitope tag; NLG(432-648), the esterase-truncated 71-residue extracellular domain, the 19-residue predicted transmembrane domain and the 127-residue C terminus of mouse neuroligin-1 (ref. 46); ERXL, the peptide sequence KSRITSEGEYIPLDQIDINVGGSGFCYENEV, a fusion of the trafficking and endoplasmic reticulum export signals from Kir2.1 (ref. 47). Other elements as above.
- aavCAG-^{dd}HTP$_{NLG(432-648)ERXL}$-2A-dTomato-WPRE. Coding: SS$_{nlg}$-HA-^{dd}HTP- NLG(432-648)-ERXL. Elements all as above.

LSPR

Localized surface plasmon resonance (LSPR) data was collected on Nicoya Alto-16 instrument using single-sequence kinetic (SSK) surface capture titration protocol, where the surface-bound protein (GFP-tagged HTP) was presented with the analytes (biotin-PEG$_{12}$-HTL.1 or biotin-PEG$_{12}$-HTL.2) sequentially with threefold increased concentration for 5 min per dose. A total of four cycles were performed on 16-channel carboxyl cartridge (Nicoya) with the single dissociation and surface regeneration steps between the cycles. Each sample channel was coupled with a negative control reference (^{dd}HTP).

Proteins were prepared as follows: pRSET T7 expression vectors containing GFP-^{dd}HTP/GFP-HTP and HisTag sequences were transformed into chemically competent *E. coli* cells and plated on carbenicillin-Luria-Bertani agar plates overnight at 37 °C. A 100 ml of MagicMedia *E. coli* expression media (Invitrogen) containing 100 mg l^{-1} carbenicillin disodium salt (Sigma) were inoculated with the *E. coli* colony. The cultures were incubated at 32 °C and shaking at 300 rpm for up to 72 h. The fluorescent GFP tag was used as indicator for protein expression. The cultures were aliquoted into 15-ml tubes. The GFP-HTP and GFP-^{dd}HTP proteins were purified using Capturem His-Tagged Purification Maxiprep kit (Takara) according to manufacturer's protocol. The elution buffer was exchanged to PBS-T buffer (Nicoya) and the samples were concentrated using Amicon 10K Centrifugal filters (Millipore). Protein concentration was measured via Qubit using Qubit Protein Assay kit. Volumes of 100 µl of 2 µM of GFP-HTP and GFP-^{dd}HTP samples were prepared in PBS-T.

Surface capture binding and/or regeneration conditions were as follows: VHH:GFP (Chromotek 1 g l^{-1}) was diluted 20 times in 10 mM sodium acetate, pH 5.5, and immobilized onto EDC/NHS-activated carboxyl sensors for 5 min, according to Nicoya surface modification protocol. Then, 2 µM GFP-tagged HTP was introduced into the VHH:GFP modified channels for 10 min and washed with PBS-T for 13 min. The regeneration of the sensor was performed by removing the GFP-HTP protein using 10 mM Glycine HCl, pH 1.5, for 5 min. The regenerated VHH:GFP surface was incubated with 2 µM GFP-tagged HTP protein for the next SSK cycle.

Analytes were prepared as follows: HTL.1: 37.5 µl of 120 µM biotin-PEG$_{12}$-HTL.1 was incubated with 2.5 µl of 1 mg ml^{-1} SA (Nicoya)

in PBS-T buffer for 60 min at room temperature. During the SSK titration protocol, the analyte was sequentially applied to the sensor at concentrations ranging from 370 nM to 30 µM (5 min per dose, via digital micro-fluidics). HTL.2: 50 µl of 3.5 µM biotin-PEG_{12}-HTL.2 analyte in PBS-T buffer was incubated with 2.5 µl of 1 mg ml^{-1} SA for 60 min at room temperature. During the SSK titration protocol, the analyte was applied to the sensor at concentrations ranging from 1.36 nM to 1.1 µM (5 min per dose, via digital micro-fluidics). Data were fit to a first-order binding model, providing an estimate of the association constant (shown in Fig. 2).

Hippocampal cultured neurons

Mixed glial and neuronal cultures were prepared from the hippocampus of postnatal day 0 to 1 Sprague–Dawley rat littermates. Pups were decapitated and brains quickly excised into ice-cold neural dissection solution (NDS), consisting of HEPES-buffered HBSS, pH 7.4 (Sigma, cat. no. H3375; Gibco, cat. no. 24020-117). Hippocampal tissue was dissected and transferred to a separate petri dish containing ice-cold NDS, quartered and washed several times with fresh ice-cold NDS. The hippocampal pieces were collected and incubated in papain enzyme (Worthington, cat. no. PAP2; 105 U per preparation in NDS) in a 37 °C water bath for 25–35 min, inverted to mix twice during incubation. The papain solution was decanted, and the tissue was washed three times in plating medium, consisting of MEM (Gibco, cat. no. 51200-038) with 10% (v:v) heat-inactivated fetal bovine serum (HyClone, cat. no. SH30071.03) and 27.8 mM glucose, 2.4 mM $NaHCO_3$, 0.1 mg ml^{-1} transferrin, 0.025 mg ml^{-1} insulin and 1% (v:v; 2 mM) L-glutamine plus 1% (v:v) penicillin–streptomycin. The tissue was further dissociated via mechanical trituration through a 10 ml serological pipette, followed by two fire-polished glass pipettes and the final cell suspension was filtered through a 0.22 µm cellulose acetate membrane.

Cells were nucleofected (Lonza, cat. no. V4SP-3096) with a selection of high-quality plasmid constructs (0.8–1 µg DNA per cuvette). After a 10-min recovery period, cells were plated individually or mixed with a different pool of cells (for cocultures). Cells were cultured on coverslips (Deckglaser) pretreated with high molecular weight poly-D-lysine (Sigma, cat. no. P7405; 0.05 mg ml^{-1}) in 24-well plates and maintained in NbActiv4 (BrainBits, NB4) at 37 °C, 5% CO_2. Media was changed by half at day in vitro (DIV) 3 or DIV4 and then weekly thereafter; experiments were performed between DIV16 and 18.

For all neuronal assays, coverslips were first rinsed briefly in a resting Tyrode solution containing (in mM): 4 KCl, 2 $CaCl_2$, 2 $MgCl_2$, 150 NaCl, 10 HEPES, 10 glucose, pH 7.4, before transfer to a glass-bottom, 24-well imaging plate (Cellvis, cat. no. P24-1.5H-N). Live cell imaging was performed on an Olympus IX83 inverted fluorescent microscope (UPlanSApo ×10 objective, numerical aperture (NA) 0.40) with Spectra X light emitting diode (LED) illumination and filter cubes as follows: (1) DAPI (4,6-diamidino-2-phenylindole): LED 395/25, excitation 387/11, Dic-409, emission 447/60; (2) GFP: LED-470/24, excitation 472/30, Dic-495, emission 520/35; (3) TRITC: LED-550/15, excitation 543/22, Dic-562, emission 593/40 and (4) Cy5: LED-640/30, excitation 628/40, Dic-660, emission 692/40.

Cultured neuronal assays

Biotin-HTL. Neurons were nucleofected with aavCAG-$^{+}HTP_{NLG(432-648)ERXL}$-2A-dTomato-WPRE, plated and cultured for 2 weeks. A dilution series was made for the biotin-PEG_{12}-HTL.1 and biotin-PEG_{12}-HTL.2 compounds in Tyrode solution containing 1% BSA, representing 12 final concentrations (in µM) between 10 and 0.001. After a brief rinse in Tyrode +BSA to acclimate the live neurons to room temperature, each coverslip was incubated in one of the 12 dilutions for 15 min, washed twice in Tyrode +BSA, then incubated in a 1:500 dilution of Streptavidin-AlexaFluor488 (2 mg ml^{-1}; Life Technologies, cat. no. S11223) for 15 min. The neurons were rinsed four times then transferred to a glass-bottom imaging plate containing Tyrode +BSA. Each coverslip was imaged in its entirety by stitching together several ×10 images (TRITC at 10 ms; GFP at 100 ms) using the Olympus CellSens software stitching algorithm. A dose–response curve was created using a custom MATLAB algorithm, involving two steps: segmentation and estimation of the fraction of HTP bound to HTL, as follows.

Regarding segmentation, we used an automated method given the number of cells per coverslip (thousands). We used the red dTomato channel (genetic expression) for segmentation, reserving the green streptavidin channel (surface HTL) as the readout. The dTomato intensity was first normalized to a 0 to 1 scale, with gamma of 0.4 to enable detection of dim cells. We performed adaptive background subtraction (90-pixel radius), applied a fixed threshold of 0.15 to obtain a binary mask, applied an open radius of 9 pixels, and detected regions with the 'regionprops' command from the MATLAB Image Processing Toolkit. This typically yielded >1,000 regions per coverslip. The quality of segmentation was confirmed by visual inspection; ~80% of regions corresponded to individual neuronal cell bodies, with the remaining being cell clusters or processes. For each region, we calculated the mean dTomato (red, R) and streptavidin (green, G) intensities.

With regard to estimating the fraction of HTP bound to HTL, data from coverslips that had been incubated in high-dose biotin-PEG_{12}-HTL.2 (≥300 nM × 15 min) appeared to be fully saturated, and were used to estimate the relationship between red (R) and green (G), which fit well to $G = G_{max} \times R/(R + R_{half})$. We interpret this equation to reflect surface trafficking of HTP, which saturates as genetic expression rises. Because all coverslips used the identical genetic construct, we took the estimates of G_{max} and R_{half} from the saturated coverslips as a constant (held fixed for all coverslips). We then fit data from each coverslip to the equation $G = HTP_{FracBound} \times G_{max} \times R/(R + R_{half})$. We used the 'fit' command from the MATLAB Curve Fitting Toolbox, which provides a nonlinear regression estimate of the only free parameter, $HTP_{FracBound}$. This estimate includes a 95% CI, which we plot as the error bars in Fig. 2a.

Rx^{DART} with biotin-DART chaser. Hippocampal neurons were nucleofected and cultured similar to the HTL assay above. A dilution series was made for YM90K.$1^{-DART.2}$, CMPDA.$2^{-DART.2}$, gabazine.$1^{-DART.2}$, diazepam.$1^{-DART.2}$, as well as Alexa647.$1^{-DART.2}$, representing seven final concentrations (in µM) between 1 and 0.001. Coverslips containing the ^{+}HTP cells were incubated in one of the seven dilutions for 15 min, washed once in Tyrode +BSA, incubated in a 1 µM solution of $biotin^{-DART.2}$ for 15 min, washed twice, then incubated in a 1:500 dilution of Streptavidin-AlexaFluor488 (2 mg ml^{-1}) for 15 min. The neurons were rinsed twice and then transferred to a glass-bottom imaging plate containing Tyrode +BSA. Each coverslip was imaged and results analyzed in a similar way to that described above.

All-optical cultured-neuron AMPAR assay

Two pools of dissociated neurons were nucleofected separately to express either:

(1) aavSYN-ChR2-HA-dsfGFP-WPRE (ChR2)
(2) aavCAG-$^{+}HTP_{NLG(432-648)ERXL}$-2A-dTomato-WPRE + aavCAG-GCaMP6s-WPRE (HTP/GC)

The ChR2 transfected cells were then mixed equally with the HTP/GC cells, plated and cultured for 16–18 days. The assay was performed in Tyrode (described above) supplemented with 10 µM CPP (NMDAR antagonist) and 10 µM gabazine ($GABA_AR$ antagonist). This recipe isolates the AMPAR, and is thus named $Tyrode^{AMPAR}$. The assay is synaptic and AMPAR-specific because we ensure that ChR2 and GCaMP6s are expressed in separate cells, such that light must first stimulate 'presynaptic' ChR2 neurons to release glutamate, which then activates 'postsynaptic' HTP/GC neurons only via the AMPAR (isolated via $Tyrode^{AMPAR}$). Thus, light-evoked HTP/GC activity is a proxy for postsynaptic AMPAR function.

We performed assays 12 coverslips at a time. Plates were removed from the incubator, coverslips briefly rinsed in $Tyrode^{AMPAR}$ and

transferred to a glass-bottom imaging plate with 500 µl of Tyrode^{AMPAR} per well. A parallel drug plate with 500 µl of Tyrode^{AMPAR} per well was used to add reagents via manual pipetting. Between dosing rounds, each well of the drug plate was mixed with its corresponding well in the imaging plate (add, gently triturate once, remove). Thus, the imaging plate maintained a set volume, and we had independent control over drug additions in each well. Overall, we performed six dosing rounds. We began with two controls (no Rx^{DART}, with mixing) to assess assay stability, followed by three drug rounds (YM90K^{DART}, with mixing) and a final wash (mix six times with fresh Tyrode^{AMPAR}). The entire assay lasted ~2 h (20 min per dose × 6 dosing rounds). We settled on three YM90K^{DART} concentrations per coverslip to balance throughput and cell health. To obtain a nine-point dose–response, we distributed doses 1:9 over coverslips A, B, C (with A = 1, 4, 7; B = 2, 5, 8; C = 3, 6, 9).

Each 20-min dosing round involved roughly 4 min of pipetting, 4 min of waiting and 12 min of optogenetic imaging. The optogenetic protocol visited each well once every 2 min for 12 min (that is, six repetitions), and thus there were 72 stage movements (12 wells × six repetitions). After each stage movement, we obtained a dTomato image (TRITC channel) followed by an optogenetic pulse train (GFP channel, 16 pulses at 3 Hz, 50 ms per pulse). We typically saw a rise in the GCaMP signal over the 16-pulse (5 s) train, with dynamics that were largely reproduced on each of the six repetitions. As described below ('Data analysis'), response variability over repetitions provided a quality-control metric, and we used the average of the last four repetitions to correspond to a roughly 15-min Rx^{DART} incubation (since pipetting midpoint).

Analysis was performed in custom MATLAB code in four steps. First we performed image alignment using the dTomato channel to account for stage jitter and coverslip drift. Second, cell bodies were segmented using a static image composed of dTomato and $\Delta F/F$ from the first control dosing round. Thus, segmentation was performed without knowledge of the GCaMP6s changes over subsequent doses. We used a combination of automated and manual segmentation, and we proofread each cell to ensure exclusion of pixels wherein cells overlap. Third, we calculated the GCaMP6s waveform for each cell by obtaining the raw trace (mean over segmented pixels of each frame), baseline subtracting (to define 0), and normalizing (to define 1). We accounted for a small amount of photobleaching by allowing the baseline to vary with time (a linear fit to the first timepoint of each pulse train). We also accounted for assay rundown so that the three YM90K^{DART} doses on a coverslip could be compared fairly. The correction factors were mild: 0.92, 0.84 and 0.82 (1.0 would reflect no rundown), and were estimated from mock assays with no Rx^{DART}. Fourth, we applied inclusion criteria to restrict analysis to cells with GCaMP expression within 1×10^3–1×10^4 AFU and with <50% change in activity in the two control doses. Cells with dTomato >$1 \times 10^{4.5}$ AFU were designated $^{+}$HTP and used to determine CC_{50} curves Fig. 2d,e. Cells with dTomato <$1 \times 10^{2.5}$ AFU were designated $^{-}$HTP. A subset of experiments were performed with aavCAG-^{dd}HTP$_{NLG(432-648)ERXL}$-2A-dTomato-WPRE (^{dd}HTP); we saw no difference between ^{dd}HTP and $^{-}$HTP data, and the data were combined to produce the AC_{50} curves in Fig. 2d,e.

With regard to the statistical unit, neurons on a coverslip were highly correlated, such that most of the variance was at the level of coverslips rather than cells. This likely reflects the synaptic nature of the assay, wherein cells are highly interconnected. As such, we defined a statistical unit as the coverslip, and we weighted the n of each cell so that each coverslip could contribute at most $n = 1$ to the AC_{50} curve, and $n = 1$ to the CC_{50} dataset. The data thus represented mean ± s.e.m. over coverslips. All data were obtained with experimental groups tested side by side, such that comparison groups were equally represented in each batch of cells.

All-optical cultured-neuron GABA$_A$R assay

Dissociated neurons were nucleofected with aavCAG-$^{+}$HTP$_{NLG(432-648)ERXL}$-2A-dTomato-WPRE + aavSYN-ChR2-HA-dsfGFP-WPRE + aavCAG-GCaMP6s-WPRE. Thus, all three elements (HTP, ChR and GC) were in the same cell. Neurons were plated on coverslips and cultured until the assay was performed at 16–18 DIV. We used Tyrode (described above) supplemented with 10 µM CPP (NMDAR antagonist) and 10 µM NBQX (AMPAR antagonist) and 10 µM GABA (low-dose GABA$_A$R agonist). This combination isolated and further activated endogenous GABA$_A$Rs and was thus named Tyrode$^{GABAR+10}$. The underlying principle of the assay is that ChR2 is the only source of excitation for a cell (all excitatory synapses blocked) yet endogenous GABA$_A$Rs largely overpower ChR2. We thus took blunted light-triggered activity as an indication of active endogenous GABA$_A$Rs, and the reinstatement of light-triggered activity as an indication of GABA$_A$R antagonism. The assay was otherwise similar to the AMPAR assay.

With regard to dosing, we performed two control rounds (no Rx^{DART}, with mixing) to establish stability, and three drug rounds (gabazine^{DART}, with mixing). However, in lieu of a wash, we used a high dose of regular gabazine (30 µM) as the sixth dosing round to serve as a calibration for the maximal neural activity (and thus the lowest GABA$_A$R function). Imaging was identical to the AMPAR assay, with a dTomato image (TRITC channel) followed by optogenetic stimulation and/or recording (GFP channel, six pulses at 3 Hz, 50 ms per pulse), with all 12 stage positions visited six times during a single dosing round. Analysis was performed in custom MATLAB code, following the same procedure for the AMPAR assay. The key difference is in regard to the statistical unit, as we found that neurons on a coverslip were not correlated, such that most of the variance was at the level of neurons rather than coverslips. This likely reflects the cell-autonomous (nonsynaptic) nature of the assay, wherein all excitatory synapses are blocked. Hence, we define a statistical unit as the neuron, and plot mean ± s.e.m. over neurons. As before, experimental groups were tested side by side, such that comparison groups were equally represented in each batch of cells.

To assay GABA$_A$R PAMs, we used a modified Tyrode$^{GABAR+3}$, with a lowered 3 µM GABA level so that ChR2 was not overpowered to start, but became overpowered on positive allostery of the GABA$_A$R. Regarding the dosing scheme, we performed only one control round (no Rx^{DART}, with mixing) and three drug rounds (diazepam^{DART}, with mixing). We next applied regular diazepam (1 µM) to establish a positive control for a full-strength PAM, followed by the sixth and final dose in which we applied gabazine (30 µM) to block all GABA$_A$Rs. Imaging alignment, proof-reading and analysis were performed in a similar fashion to the GABAR assay using MATLAB. As with the gabazine assay, a statistical unit was a neuron, and we plotted mean ± s.e.m. over neurons. Experimental groups were tested side by side, such that comparison groups were equally represented in each batch of cells. In particular, given a lower overall signal to noise in the GABA$_A$R PAM assay, we ran side-by-side groups wherein Rx^{DART} was replaced with a negative control (no drug) or positive control (regular diazepam) to account for assay stability over time (Extended Data Fig. 6a).

Dual-patch recording

The unitary excitatory postsynaptic potentials were recorded in cultured hippocampal neurons 3 weeks after plating, with dual-patch recording configuration. To elicit postsynaptic unitary excitatory postsynaptic potentials (uEPSP), the two cells were both under whole-cell current-clamp mode, induced one single action potential at presynaptic cell (^{dd}HTP or $^{+}$HTP) to stimulate neighboring cell ($^{+}$HTP or ^{dd}HTP) that synaptically connected with presynaptic cell.

Recombinant adeno-associated viral vectors

All custom viral vectors were produced by the Duke Viral Vector Core. Human embryonic kidney 293 cells were transfected with a triple transient transfection protocol of the adenovirus helper plasmid, the AAV helper plasmid and the inverted terminal repeat transgene cassette plasmid. The adenovirus helper cassettes encodes the adenovirus proteins (E1A, E1B, E4 and E3A) and the adenovirus virus-associated

RNAs required for helper functions. The AAV helper plasmid encodes the wild-type AAV genome lacking inverted terminal repeats. The recombinant adeno-associated viral vector was harvested from the nuclei of transfected cells 48–72 h after transfection and purified from the cell homogenate using a double round cesium chloride gradient protocol. Genome titers were estimated using real time PCR.

Acute brain slice preparation

DAT-IRES-Cre mice (six males, three females, 8–10 weeks) were injected with either AAV_{rh10}-CAG-DIO-$^{+}HTP_{GPI}$-2A-dTomato-WPRE or AAV_{rh10}-CAG-DIO-$^{dd}HTP_{GPI}$-2A-dTomato-WPRE (2×10^{12} VG ml^{-1}, 100 nl per site at −3.2 mm anteroposterior, ±0.5 mm mediolateral, −5.0/−4.5 mm dorsoventral). After 3–5 weeks for expression, mice were deeply anesthetized with isoflurane and euthanized by decapitation. Coronal brain slices (300 µm) containing VTA were prepared by standard methods using a Vibratome (Leica, VT1200S), in ice-cold high sucrose cutting solution containing (in mM): 220 sucrose, 3 KCl, 1.25 NaH_2PO4, 25 $NaHCO_3$, 12 $MgSO_4.7H_2O$, 10 glucose and 0.2 $CaCl_2$ bubbled with 95% O_2 and 5% CO_2. The slices were placed into modified artificial cerebrospinal fluid (ACSF) containing (in mM): 120 NaCl, 3.3 KCl, 1.23 NaH_2PO_4, 1 $MgSO_4$, 2 $CaCl_2$, 25 $NaHCO_3$ and 10 glucose at pH 7.3, previously saturated with 95% O_2 and 5% CO_2. For recovery, the slices were incubated at 33 °C for 40–60 min in the bubbled ACSF solution and then allowed to cool to room temperature (22–24 °C) until the recordings were initiated.

Retinal whole-mount preparation

PV-Cre mice (22 males, 38 females, 12–24 weeks) were intravitreally injected with either AAV_{7m8}-CAG-DIO-$^{+}HTP_{GPI}$-2A-dTomato-WPRE or AAV_{7m8}-CAG-DIO-$^{dd}HTP_{GPI}$-2A-dTomato-WPRE (4.4×10^{11} VG ml^{-1}, 1.0 µl per eye). After 8–12 weeks, the mice were euthanized by cervical dislocation. Both eyes were removed and dissected under a stereo-microscope. Retinas were isolated from the eyecups and placed in oxygenated (95% O_2 and 5% CO_2) cold-Ames medium (Sigma-Aldrich), supplemented with 21 mM $NaHCO_3$. After the vitreous body was removed, a retina was cut into three pieces, leaving each retina piece attached to a filter paper with 2-mm hole by retina ganglion cell-side down. The pieces of retina were stored in bubbled Ames solution at room temperature, then transferred to the recording chamber with retina ganglion cell-side up for recording.

Acute brain slice and retina electrophysiology

The brain slices or retinas were perfused with bubbled ACSF at 29–30 °C with a 2 ml min^{-1} flow rate. Recordings were made by whole-cell patch recording techniques using a Multiclamp 700B amplifier (Molecular Devices, Axon Instruments Inc.). The signals were filtered at 10 kHz and acquired using a Digitate 1440A and pClamp 10.7 (Molecular Devices). The recording pipettes (4–6 MΩ) were filled with internal solutions. To measure $GABA_AR$ IPSC, the pipettes were filled with a cesium chloride-based internal solution (in mM): 135 CsCl, 2 $MgCl_2$, 0.5 EGTA, 10 HEPES, 4 Mg-ATP, 0.5 Na-GTP, 10 Na_2-phosphocreatine and 4 QX314 (lidocaine *N*-ethyl bromide), pH adjusted to 7.3 with CsOH (290 mOsm). For AMPAR-mediated EPSC recording, the pipette solution contained (in mM) 130 CsMeS, 1 $MgCl_2$, 0.5 EGTA, 10 HEPES, 4 Mg-ATP, 0.5 Na-GTP, 10 Na_2-phosphocreatine, and 4 QX314, pH adjusted to 7.3 with CsOH (290 mOsm). Evoked-IPSC or -EPSC signals were elicited by electrical stimuli of 0.3 ms duration and 150–300 µA (60–70% maximum responses), with a repetition interval of 15 s. The stimulating electrode was placed 60–100 µm from the recorded neuron. $GABA_AR$-mediated IPSCs were isolated in the presence of DNQX (20 µM, AMPAR antagonist) and AP-V (50 µM, NMDA antagonist) in the bath solution. For AMPAR-mediated EPSCs, picrotoxin (50 µM, $GABA_AR$ antagonist) and AP-V (50 µM, NMDAR antagonist) were added to the bath solution. For current-clamp recording, the pipette solution contained (in mM) 130 K-gluconate, 5 KCl, 2 $MgCl_2$, 0.2 EGTA, 10 HEPES, 4 Mg-ATP, 0.5 Na-GTP and 10 phosphocreatine, pH adjusted to 7.3 with KOH (290 mOsm). The liquid junction potential was estimated to be 15.9 mV for the normal ACSF solution and was not corrected. Our inclusion criteria required that cells maintain stable access and holding currents for at least 5 min. In particular, series resistance is monitored using 5–10-mV hyperpolarizing steps interleaved with our stimuli, and cells are discarded if series resistance changed more than roughly 15% during the experiment. The stored data signals were processed using Clampfit v.10.7 (Axon Instruments). All averaged data are presented as mean ± s.e.m. and *n* represents the number of cells tested per condition. Statistical significance was determined using Student's *t* or one- or two-way analysis of variance tests. IPSC or EPSC decay time constants were obtained by fitting a single-exponential function, $I(t) = I\exp^{(-t/\tau)} + I_{SS}$, where $I(t)$ is the amplitude of the current at time t and I_{SS} is the steady-state current, I is instantaneous current subtracted from I_{SS} and t is the time constant of decay.

Cerebellum experiments

BACα6Cre-C × Ai148D-Cre mice (six males, four females, P50–60) were given a 3-mm diameter craniotomy over Crus I at approximately 3.0 mm lateral and 4.3 mm posterior to lambda. Crus I was injected (WPI UMP3) with 150 nl of either AAV_{7m8}-CAG-DIO-$^{+}HTP_{GPI}$-2A-dTomato-WPRE (1×10^{12} VG ml^{-1}) or AAV_{7M8}-CAG-DIO-$^{dd}HTP_{GPI}$-2A-dTomato-WPRE (1×10^{12} VG ml^{-1}) at a rate of 30 nl min^{-1} and a depth of 350 µm at 2–3 sites. Glass windows consisting of two 3-mm coverslips bonded to a 5-mm coverslip (Warner Instruments No. 1) with index-matched adhesive (Norland No. 1) were installed in the craniotomy using Metabond. Imaging mice receiving saline and drug infusions received a plastic cannula (Plastics One; C315GS/PK length 0.5 mm) positioned immediately rostral to the imaging window and attached with Metabond. All mice were individually housed after cannula placement and given 8 weeks to allow viral expression, including 1–2 weeks of habituation to head restraint.

Imaging was performed with a resonant scanning microscope (Neurolabware) equipped with a ×16 water-immersion objective (Nikon CF175 LWD 16xW 0.8 NA). The cerebellum was scanned with a TI:Sapphire laser tuned to 920 nm (SpectraPhysics, Mai Tai eHP DeepSee) using a resonant galvanometer (8 kHz, Cambridge Technology) at a frame rate of 30 Hz and a field of view of 278 × 117 µm (796 × 264 pixels). Data were collected through a green filter (510 ± 42 nm band filter (SEMrock)) onto GaAsP photomultipliers (cat. no. H10770B-40, Hamamatsu). Throughout imaging, a polymer (MakingCosmetics, 0.4% Carbomer 940) was used to stabilize the immersion solution. Images were processed using the open-source Python toolbox for large scale calcium imaging data analysis CaImAn[48] and custom written MATLAB code, as previously described[26]. Cerebellar slice preparation and granule cell voltage-clamp recordings were performed as described previously[26] using tissue from BACα6Cre-C mice injected with the same AAVs used for in vivo experiments (above) to drive ^{+}HTP and ^{dd}HTP expression.

VTA_{DA} locomotion experiments

Adult DAT-IRES-cre mice (20 males, 18 females; 10–20 weeks old) were anesthetized and stereotactically injected with 400 nl of either AAV_{rh10}-CAG-DIO-$^{+}HTP_{GPI}$-2A-dTomato-WPRE or AAV_{rh10}-CAG-DIO-$^{dd}HTP_{GPI}$-2A-dTomato-WPRE (2×10^{12} VG ml^{-1}, 100 nl per site, two tracks with two depths per track: −3.2 mm anteroposterior, ±0.5 mm ML, −5.0/−4.5 mm dorsoventral) and immediately implanted with a bilateral metal cannula above the VTA (P1Tech; C235G-1.0) lowered to −3.75 mm. Mice were fitted with a plastic head bar adhered to the skull with ultraviolet glue and dental cement, enabling head fixation to facilitate drug infusions in awake animals. Assays were performed at least 3 weeks after viral injection to allow for recombinant protein expression. Mice were singly housed postsurgery, in a 12-h reverse light cycle, with food and water provided ad libitum. Mice were acclimated to head fixation for three consecutive days before behavioral experiments.

Mice were head fixed on a round plastic treadmill (Delvie's Plastics, 8-inch plexiglass disk covered with silicone rubber) attached to a rotary encoder to collect rotation data (US Digital, cat. no. H5-100-NE-S). Rotary encoder data was collected by a National Instruments card (NI USB-6351 X Series DAQ) and a custom MATLAB script. Mice were water restricted to 80–85% body weight and delivered occasional sucrose rewards (Lee Company solenoid, cat. no. LHDA1233315H HDI-PTD-Saline-12V-30PSI) to induce motivation to run. Behavior sessions consisted of 1 h per day on consecutive days. After ten baseline running sessions to fully acclimate to the treadmill, mice had reagents infused into the brain via the cranial cannula as previously described[3]. DART reagents were freshly thawed and diluted in sterile ACSF to 10 µM gabazine.7$^{DART.2}$ + 1 µM Alexa647.1$^{DART.2}$, with 0.6 or 0.8 nl per hemisphere infused at a rate of 0.1 µl min^{-1}. Mice were then recorded on the treadmill at 2 and 24 h postinfusion. Wheel speed was analyzed by a custom MATLAB script, and was normalized per mouse to their average wheel speed during the final training session.

Open-field turning assay

Adult (10–20 weeks old) Drd1a-Cre mice (six males, eight females) were anesthetized and stereotactically injected with 960 nl of AAV$_{rh10}$-CAG-DIO-$^{+}$HTP$_{GPI}$-2A-dTomato-WPRE or AAV$_{rh10}$-CAG-DIO-^{dd}HTP$_{GPI}$-2A-dTomato-WPRE (2×10^{12} VG ml^{-1}, 80 nl per site, four tracks with three depths per track: 0.55 mm anteroposterior, −1.7 mm mediolateral, −2.8/−2.3/−1.8 mm dorsoventral; 1.35 mm anteroposterior, −1.3 mm mediolateral, −3.0/−2.5/−2.0 mm dorsoventral; 1.45 mm anteroposterior, −2.1 mm mediolateral, −3.1/−2.6/−2.1 mm dorsoventral; 0.65 mm anteroposterior, −2.5 mm mediolateral, −3.1/−2.6/2.1 mm dorsoventral); we found that distributed injections of lower volumes of virus resulted in consistent and robust expression without toxicity. Mice were immediately implanted with a plastic (peek) cannula (P1Tech, C315G/PK) at −1.9 mm mediolateral and 1.0 mm anteroposterior lowered to −2.5 mm; peek was favored for these experiments to eliminate the hypothetical possibility that nitroaromatic compounds such as YM90K could be reduced by iron-containing surfaces. Mice were fitted with a plastic head bar adhered to the skull with ultraviolet glue and dental cement, enabling head fixation to facilitate drug infusions in awake animals.

Reagents were infused into the brain via the cranial cannula as previously described[3]. Following infusion, mice were placed into open-field chambers (27 × 27 cm) in the dark, and behavior was recorded using infrared video. The positions of the nose, tail and center of mass of each mouse were tracked using Noldus Ethovision XT 10, and analyzed offline in custom MATLAB scripts. Changes in orientation of the vector pointing from tail to nose were analyzed to identify vector rotations of at least 360° with no more than 25% cumulative rotation in the opposite direction (for example, a 400° rotation to the right could contain no more than 100° cumulative hesitations to the left). Rotations were normalized (for example, 400°/360° = 1.11 turns). False rotations attributed to nose to tail assignment flips were eliminated by excluding frames in which the nose-tail distance decreased to less than half of the median value. Left and right rotations were separately tallied, and net turns (for example, Fig. 4c) is total left minus right turns per hour. For analysis of rotations binned according to turn diameter (for example, Fig. 4d), a sliding-window analysis was performed over each 360° portion of a turn; diameter was defined as the maximum Euclidean distance between all center of mass positions. Separate histograms were tallied for left and right turns.

Dorsal striatum histology

Mice were deeply anesthetized with isoflurane and fixed by transcardial perfusion of 15 ml of PBS followed by 50 ml ice-cold 4% paraformaldehyde (PFA) in 0.1 M PB, pH 7.4. Brains were excised from the skull, further postfixed in 50 ml of 4% PFA at 4 °C overnight then washed three times with PBS. Brains were embedded in 5% agarose and sliced along the coronal axis at 50 µM (Leica, cat. no. VT1200S). Sections were mounted onto glass slides (VWR, cat. no. 48311-703) and coverslipped with Vectashield mounting medium (Vector Laboratories, cat. nos. H-1400 or H-1800). Fluorescent images (DAPI, GFP, TRITC, Cy5) were collected at ×10 magnification with either an Olympus IX83 inverted microscope or an Olympus VS200 slide scanner. Images were analyzed for pixel intensity using MATLAB. For each coronal section, the striatum was manually segmented in both hemispheres. Background fluorescence (median of the right, control hemisphere) was subtracted. Dye capture in the left hemisphere was calculated via a pixel-wise summation over 25 coronal sections (cannula center ±12 sections; 50 µm per section).

Visual cortex surgeries

SOM::Cre mice (2 males, 1 female, for two-photon experiments) of a 50% CBA/CaJ background, or CBA mice (two males, for ambient pharmacokinetic experiments) aged >P45 were administered dexamethasone (3.2 mg kg^{-1}, subcutaneously (s.c.)) <2 h before surgery. Mice were anesthetized with isoflurane (1.25–2% in 100% O_2), ketamine (200 mg kg^{-1}, intraperitoneal (i.p.)) and xylazine (30 mg kg^{-1}, i.p.), then an incision was made in the scalp and the dorsal side of the skull was scraped clean of remaining tissue. A guide cannula (cat. no. F11552, P1 Technologies) with a complementary dummy cannula (cat. no. F11372, P1 Technologies) was directed to the right lateral ventricle using the following coordinates from bregma: 1.10 mm lateral, 0.20 mm posterior and 2.30 mm from the skull surface. The cannula was secured to the skull with Metabond (Parkell).

Within the same surgery, a custom titanium headpost was cemented to the skull with Metabond and a 4.5-mm craniotomy was made over the left visual cortex centered on the following coordinates from lambda: 3.10 mm lateral and 1.64 mm anterior. The craniotomy was fit with a custom-made glass window composed of a 6-mm coverslip bonded to two 4.5-mm coverslips (Warner, no. 1) with refractive index-matched adhesive (Norland, no. 71), and the window was fixed in place with Metabond. Buprenorphine (0.05 mg kg^{-1}) and cefazolin (50 mg kg^{-1}) were delivered s.c. for 48 h following surgery. Following at least 7 days recovery from the implantation surgery, mice were gradually habituated to head restraint. Mice to be used for two-photon experiments then underwent retinotopic mapping using widefield autofluorescence imaging[49] to locate the primary visual cortex within the cranial window, which served as the target for viral injections.

The mice used for two-photon imaging underwent an additional surgery for viral injection. Dexamethasone (3.2 mg kg^{-1}, s.c.) was administered at least 2 h before surgery. After anesthesia with isoflurane (1.25–2% in 100% O_2), the cranial window was removed. AAV$_{rh10}$-CAG-DIO-$^{+}$HTP$_{GPI}$-IRES-dTomatoF-W3SL (9×10^{13} VG ml^{-1}) mixed with AAV$_9$-SYN-jGCaMP8s-WPRE (2.8×10^{13} VG ml^{-1}) in a 1:1 ratio was injected via a glass micropipette mounted on a Hamilton syringe, driving expression of HTP and dTomato in somatostatin+ interneurons while driving GCaMP expression in all neurons. Two hundred nanoliters of virus were injected at 170–230 µM below the pia (30 nl min^{-1}); the pipette was left in the brain for an additional 3 min to allow the virus to infuse into the tissue. Following injection, a new coverslip was sealed in place with Metabond. We then waited a minimum of 2 weeks for viral expression to mature before performing two-photon experiments.

Lateral ventricle pharmacokinetics

For YM90K.1$^{DART.2}$ and Alexa647.1$^{DART.2}$ delivery, mice were head fixed on a running wheel and the dummy cannula removed. An internal cannula (cat. no. F11373, P1 Technologies) connected to a Hamilton syringe on an infusion pump was inserted into the guide cannula and secured in place. Compounds were delivered at 100 nl min^{-1}, followed by a 10–20-min waiting period before the internal cannula was removed. The dummy cannula was then reinserted and secured.

We visualized Alexa647.1$^{DART.2}$ through the cranial window using widefield microscopy. An excitation wavelength of 624 ± 40 nm was

delivered through the cranial window and emitted light was filtered at 692 ± 40 nm. Images were collected using a CCD camera (Rolera EMC-2, QImaging) through a five air-immersion objective (0.14 NA, Mitutoyo), using Micromanager acquisition software (NIH) and were analyzed in imageJ (NIH) to qualitatively (for two-photon experiments) or quantitatively (for ambient pharmacokinetics experiments) measure changed in fluorescence.

Lateral ventricle pulse-chase with biotin.1$^{DART.2}$

We performed an acute local injection of biotin.1$^{DART.2}$ either 24 h after ICV (intracerebroventricular) infusion of YM90K.1$^{DART.2}$ and Alexa647.1$^{DART.2}$, or in animals that had never received an ICV bolus. Having determined the location of HTP expression in visual cortex using widefield imaging, we used vasculature landmarks to target the biotin.1$^{DART.2}$ injection to the center of this region. Dexamethasone was administered at least 2 h before surgery and animals were anesthetized with isoflurane (1.2–2% in 100% O_2). The cranial window was removed and a glass micropipette was filled with biotin.1$^{DART.2}$ (30 µM in sterile ACSF), mounted on a Hamilton syringe and lowered into the brain. Then 1 µl of biotin.1$^{DART.2}$ was injected 200–300 µm below the pia (100 nl min^{-1}); the pipette was left in the brain for an additional 10 min to allow the drug to infuse into the tissue. Following injection, a new coverslip was sealed in place. Animals recovered from anesthesia for approximately 1 h to allow DART binding, then were euthanized via intracardial perfusion with 4% PFA and the brains extracted. Brains were postfixed in 4% PFA for 24 h then cut into 50-µm sections. To visualize biotin.1$^{DART.2}$ binding, slices were incubated in in streptavidin-Alexa750 (2 µG ml^{-1} in phosphate buffered saline) for 1 h at room temperature with gentle agitation, then washed three times in phosphate buffered saline.

Visual cortex 2P imaging and analysis

Images were collected using a two-photon microscope controlled by Scanbox software (Neurolabware). A Mai Tai eHP DeepSee laser (Newport) was directed into a modulator (Conoptics) and raster scanned on the visual cortex using resonant galvanometers (8 kHz; Cambridge Technology) through a ×16 (0.8 NA, Nikon) water-immersion lens. Emitted photons were directed through a green filter (510 ± 42 nm band filter; Semrock) or a red filter (607 ± 70 nm band filter; Semrock) onto GaAsP photomultipliers (cat. no. H10770B-40, Hamamatsu). Frames were collected at 15 Hz. At the start of each experiment, an excitation wavelength of 1,040 nm was used to visualize dTomato fluorescence, allowing identification of $^{+}$HTP cells. All subsequent imaging employed an excitation wavelength of 920 nm. Mice were head fixed on running wheel, and locomotion was monitored with a digital encoder (US Digital, cat. no. H5-32-NE-S) at 10 Hz. Full-field drifting gratings in eight directions (from 0 to 315° in intervals of 45°) at three contrasts (25, 50 and 100%; data shown are for 50% contrast) were presented to the right visual field; each trial constituted a 2-s stimulus presentation and a 4-s interstimulus interval. Data were collected at 180–250 µM below the cortical surface.

Custom code written in MATLAB (MathWorks) was used to analyze two-photon data. To adjust for x–y motion, we registered all frames from each imaging session to a stable reference image selected out of several 500-frame-average images, using Fourier domain subpixel two-dimensional rigid body registration. We manually segmented cell bodies, first using the dTomato fluorescence to segment and identify $^{+}$HTP cells, then segmenting all other visible cells from images of the average $\Delta F/F$ signal during presentation of each stimulus, a time-averaged image of the full stack and a local correlation map. These later two segmentation strategies allowed detection of cells that were active only weakly visually responsive. All segmented cells that were not identified based on dTomato fluorescence were labeled as $^{-}$HTP and assumed to be putative pyramidal cells.

We derived fluorescence time courses by averaging all pixels in a cell mask. To exclude signal from the neuropil, we first selected shell around each neuron (excluding neighboring neurons), then estimated the neuropil scaling factor by maximizing the skew of the resulting subtraction and finally removed the identified component from each cell's time course. Time courses were then split into 6-s epochs corresponding to stimulus trials, and visually evoked responses were measured as the average $\Delta F/F$ in the 2-s stimulus period (where F was designated at the mean fluorescence in the 1-s period preceding the stimulus).

For each mouse we performed a baseline imaging session the day before YM90K^{DART} ICV delivery, then re-identified the same imaging field of view in a second imaging session after delivery. We matched cells across imaging sessions using a custom MATLAB script; briefly, after registration the image stack from the baseline session was rotated to fully align with the image stack from the session following drug delivery, then for each cell found in the post-ICV session we examined a small field of view in the corresponding region of the stack from the baseline session to determine whether the cell was visible in the baseline session. Among cells that we could identify in both imaging session, we included for analysis any cell that was visually responsive (demonstrated a statistically significant elevation in $\Delta F/F$ during the stimulus period for at least one stimulus condition as defined by a Bonferroni corrected paired t-test) in at least one of the sessions. We then found the preferred direction of visual grating for each cell on each day, and analyses were performed on the subset of trials at that grating direction for each cell. We further restricted the present analyses to stationary periods (wheel speed <2 cm s^{-1}).

Reporting summary

Further information on research design is available in the Nature Portfolio Reporting Summary linked to this article.

Data availability

Source data are provided for electrophysiology experiments at https://github.com/tadrosslab/DART.2. Due to their large size, raw imaging datasets are available upon request and will be fulfilled by the corresponding author.

Code availability

Codes that support the findings of this study are available at https://github.com/tadrosslab/DART.2.

References

47. Gradinaru, V. et al. Molecular and cellular approaches for diversifying and extending optogenetics. *Cell* **141**, 154–165 (2010).
48. Giovannucci, A. et al. CaImAn: an open source tool for scalable calcium imaging data analysis. *eLife* **8**, e38173 (2019).
49. Jin, M. & Glickfeld, L. L. Magnitude, time course, and specificity of rapid adaptation across mouse visual areas. *J. Neurophysiol.* **124**, 245–258 (2020).

Acknowledgements

We thank J. Roach for technical support in open-field behavioral assays and data processing; R. Carter for VTA histology analysis; I. Weaver for contributions to laboratory and surgery-station setup; T. Haimowitz for synthesis and codesign of the first batch of azide$^{DART.1}$; S. Thana for support with synthesis of CMPDA.2$^{DART.2}$; J. Izquierdo-Ferrer for contributing to the methods and partial synthesis of gabazine^{DART} reagents and M. Harnett, E. Issa, A. Choudhury, R. Ravenel and J. Hong for insightful feedback on the manuscript. This work was supported by Duke University Startup Funds (to C.H., G.D.F., L.L.G. and M.R.T.), Duke University Holland Trice Scholars Award (to L.L.G.), Duke University DIBS Awards (to M.R.T.) and by NIH grant nos. 1F3-1NS113742-01A1 (to E.A.F.); R01-NS096289 and R01-NS112917 (to C.H.); R34-NS111645 and R01-EY031396 (to G.D.F.); R01-EY031716 (to L.L.G.) and RF1-MH117055, DP2-MH1194025, R01-NS107472 and R61-DA051530 (to M.R.T.).

Author contributions

See Supplementary Table 4 for detailed author contributions. Conceptualization was carried out by B.C.S., H.Y., S.S.X.L., S.C.V.B., C.M.C., E.A.F., S.A.Y., T.M.H., C.H., G.D.F., L.L.G. and M.R.T. Methodology was developed by B.C.S., H.Y., S.S.X.L., S.C.V.B., C.M.C., E.A.F., S.A.Y., V.Z.G., E.W.K., P.P.V., M.H.L., L.Z., M.E.M., M.L.S., T.M.H., M.T., A.B.R., G.E.S., C.H., G.D.F., L.L.G. and M.R.T. Software was written by S.C.V.B. and M.R.T. Validation was done by B.C.S., H.Y., S.S.X.L., S.C.V.B., C.M.C., E.A.F., S.A.Y., V.Z.G., E.W.K., M.H.L., M.E.M., M.L.S., T.M.H., M.T. and M.R.T. Formal analysis was carried out by B.C.S., H.Y., S.C.V.B., C.M.C., E.A.F., P.P.V., L.Z., G.E.S. and M.R.T. The investigation was carried out by B.C.S., H.Y., S.S.X.L., S.C.V.B., C.M.C., E.A.F., S.A.Y., V.Z.G., E.W.K., P.P.V., M.H.L., L.Z., T.M.H., M.T. and M.R.T. Resources were provided by A.B.R., G.E.S., C.H., G.D.F., L.L.G. and M.R.T. Data were curated by B.C.S., H.Y., S.C.V.B., C.M.C., E.A.F., S.A.Y., V.Z.G., E.W.K. and M.R.T. The original draft was written by B.C.S., H.Y., S.S.X.L., C.M.C., V.Z.G., P.P.V., L.Z. and M.R.T. Writing, review and editing of the manuscript was done by B.C.S., H.Y., S.S.X.L., S.C.V.B., C.M.C., E.A.F., P.P.V., G.E.S., C.H., G.D.F., L.L.G. and M.R.T. Visualization was done by B.C.S., H.Y., S.S.X.L., S.C.V.B., C.M.C., E.A.F., V.Z.G. and M.R.T. Supervision was the responsibility of B.C.S., C.M.C., M.E.M., A.B.R., G.E.S., C.H., G.D.F., L.L.G. and M.R.T. Project administration was done by B.C.S., E.W.K., A.B.R., G.E.S., C.H., G.D.F., L.L.G. and M.R.T. Funding was acquired by E.A.F., C.H., G.D.F., L.L.G. and M.R.T.

Competing interests

M.R.T., B.C.S., A.B.R., M.H.L. and M.E.M. are on patent applications describing HTL.2 and its applications. A.B.R., M.H.L. and M.E.M. are employees of Fox Chase Chemical Diversity Center. The remaining authors declare no competing interests.

Additional information

Extended data is available for this paper at https://doi.org/10.1038/s41592-024-02292-9.

Supplementary information The online version contains supplementary material available at https://doi.org/10.1038/s41592-024-02292-9.

Correspondence and requests for materials should be addressed to Michael R. Tadross.

Peer review information *Nature Methods* thanks Johannes Broichhagen, Joshua Levitz and Alexandre Mourot for their contribution to the peer review of this work. Peer reviewer reports are available. Primary Handling Editor: Nina Vogt, in collaboration with the *Nature Methods* team.

https://doi.org/10.1038/s41592-024-02292-9

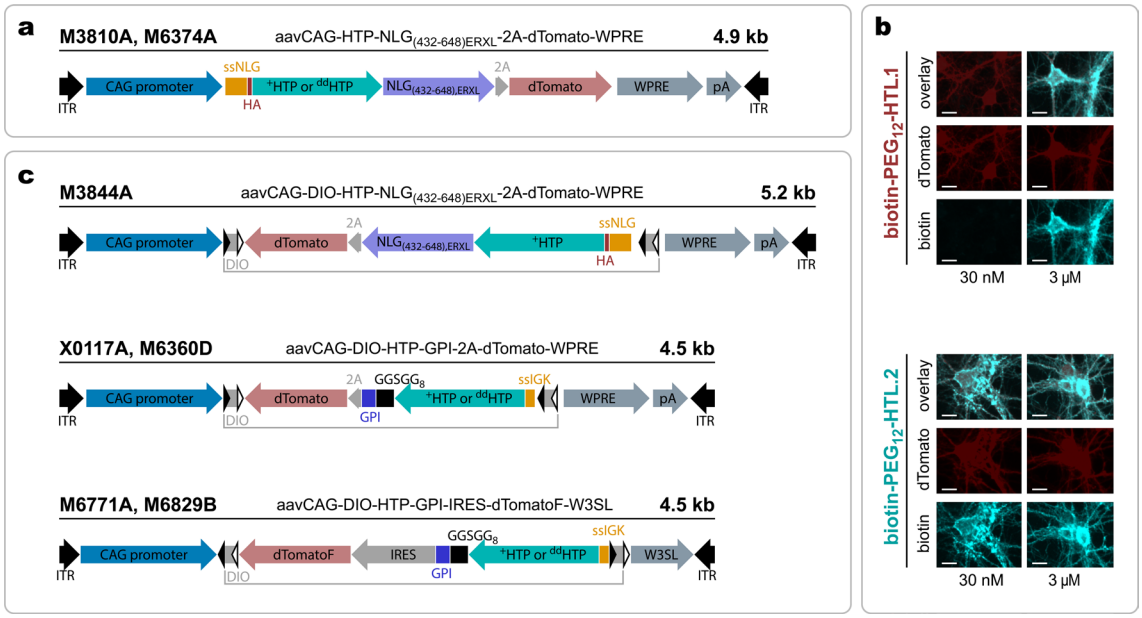

Extended Data Fig. 1 | Genetic construct design. (a) Constructs for electroporation (cultured neuron experiments). M3810 (GenBank PP719192) contains $^{+}$HTP anchored to a transmembrane $NLG_{(432\text{-}648)}$ domain, a 2A ribosomal skip sequence, and a WPRE element[3]. M6374 (GenBank PP719194) is the ^{dd}HTP version of this design. **(b) Individual color channels.** Corresponds to Fig. 2a. Scale bar 10 µm. **(c) Constructs for AAV packaging (slice and behavioral work).** M3844 (not used in this study) is a Cre-dependent version of the $NLG_{(432\text{-}648)}$ / 2A / WPRE design (5.2 kb length)[3]. X0117A (GenBank PP719197) and M6360D (GenBank PP719193) use a GPI / 2A / WPRE design (4.5 kb length). M6771A (GenBank PP719195) and M6829B (GenBank PP719196) use a GPI / IRES / W3SL design (4.5 kb length).

https://doi.org/10.1038/s41592-024-02292-9

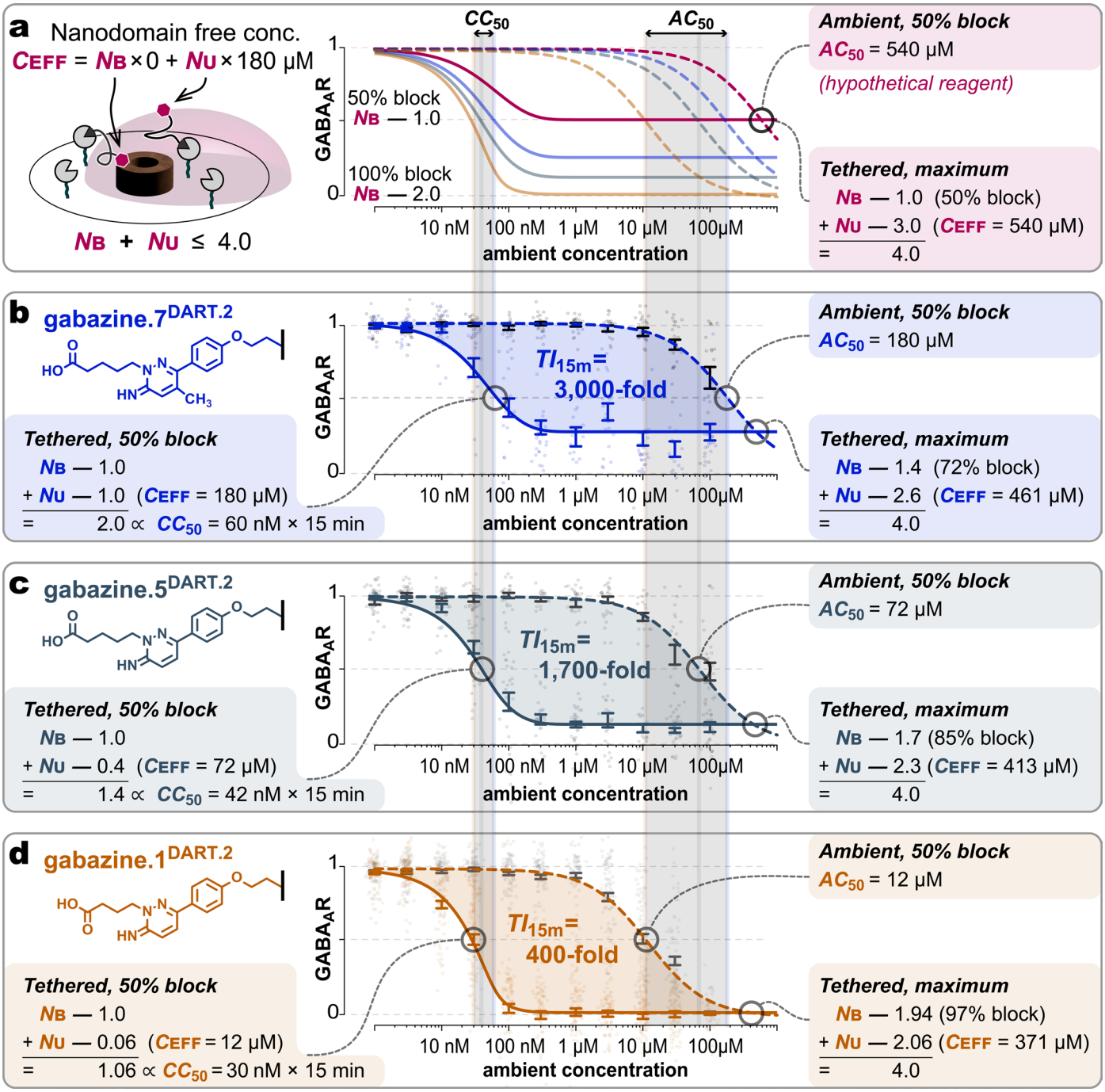

Extended Data Fig. 2 | Gabazine series and nanodomain model. Nanodomain tethered-drug model. (a) Key model parameters. The model considers only the gabazine molecules tethered to HTP proteins within 16 nm of the $GABA_AR$. N_B and N_U are the number of gabazine molecules bound and unbound to the $GABA_AR$, respectively. C_{EFF} is the effective concentration of gabazine in the nanodomain. Dose-response curve depicts hypothetical reagent with AC_{50} = 540 μM, for which CC_{50} occurs when N_B = 1 (for half-block) and N_U = 3 (for C_{EFF} = 540 μM). See Supplementary Discussion. **(b-d) Gabazine^{DART} series.** Chemical structure of each gabazine variant is shown on the top left. Dose-response relationship overlays raw data (means ± SEM of cells) with model fits shown in dashed (ambient) and solid (tethered) curves. Numerical values of N_B, N_U, and C_{EFF} are provided along the tethered dose-response curve. For gabazine.7$^{DART.2}$, CC_{50} = 60 nM × 15 min ($^{+}$HTP: n = 18 cells), AC_{50} = 180,000 nM (^{dd}HTP: n = 21 cells), TI_{15m} = 3,000-fold. For gabazine.5$^{DART.2}$, CC_{50} = 42 nM × 15 min ($^{+}$HTP: n = 25 cells), AC_{50} = 72,000 nM (^{dd}HTP: n = 23 cells), TI_{15m} = 1,700-fold. For gabazine.1$^{DART.2}$, CC_{50} = 30 nM × 15 min ($^{+}$HTP: n = 62 cells), AC_{50} = 12,000 nM (^{dd}HTP: n = 63 cells), TI_{15m} = 400-fold.

https://doi.org/10.1038/s41592-024-02292-9

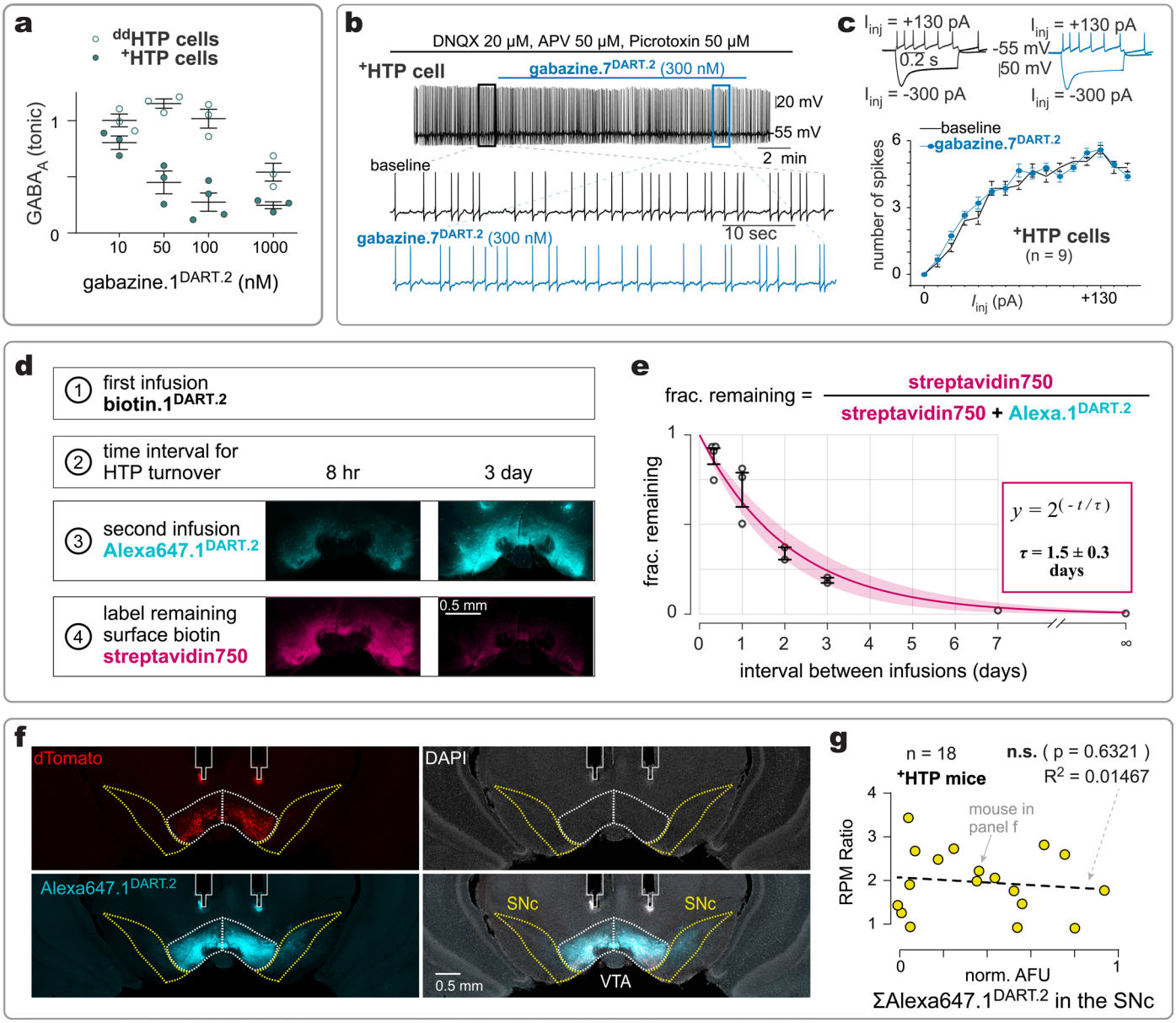

Extended Data Fig. 3 | Supporting data for gabazine behavioral experiments. (a) Cerebellar gabazine.1$^{DART.2}$ dose-response. Each symbol is an independent granule cell; error bars are mean ± SEM over cells. CC_{50} ~ 20 nM × 15 min ($^{+}$HTP cells); AC_{50} ~ 1,000 nM (^{dd}HTP cells). **(b, c) Gabazine.7$^{DART.2}$ and VTA$_{DA}$ action potentials.** Exemplar in panel b shows spontaneous action potentials of a VTA$_{DA}$ neuron in the presence of picrotoxin (GABA$_A$ blocker), DNQX (AMPA blocker) and APV (NMDA blocker). Panel c quantifies action potential firing as a function of injected current; performed before (black) and after (cyan) gabazine.7$^{DART.2}$ was tethered in each cell. Error bars are mean ± SEM over $n = 9$ $^{+}$HTP cells. Representative traces shown above. **(d, e) HTP turnover estimation.** Protocol and exemplar images (panel d): a pulse of 1.2 μL of 30 μM biotin.1$^{DART.2}$ was administered and subsequently chased (after intervals ranging from 8 hr to 7 days) with an infusion of 1.2 μL of 30 μM Alexa647.1$^{DART.2}$. Example histology shown for 8-hr and 3-day intervals. Quantification of the fraction surface biotin$^{DART.2}$ remaining vs infusion interval (panel e): each symbol is an independent mouse; error bars are mean ± SEM over mice. The data were fitted to an exponential, revealing a half-turnover of HTP protein at 1.5 ± 0.3 days (mean ± 95% CI via nonlinear least squares fitting). **(f) Quantifying VTA versus SNc ligand capture.** Histology from one exemplar mouse showing dTomato expression ($^{+}$HTP, red) and Alexa647.1$^{DART.2}$ capture (cyan). Segmentation of the VTA (white outlined region) and SNc (yellow outlined region). **(g) Locomotion vs SNc ligand capture.** Locomotor effects (RPM ratio) plotted against capture of Alexa647.1$^{DART.2}$ in the SNc of each mouse ($n = 18$ $^{+}$HTP mice). There was not a significant correlation (Pearson's $r^2 = 0.01467$; $P = 0.6321$).

https://doi.org/10.1038/s41592-024-02292-9

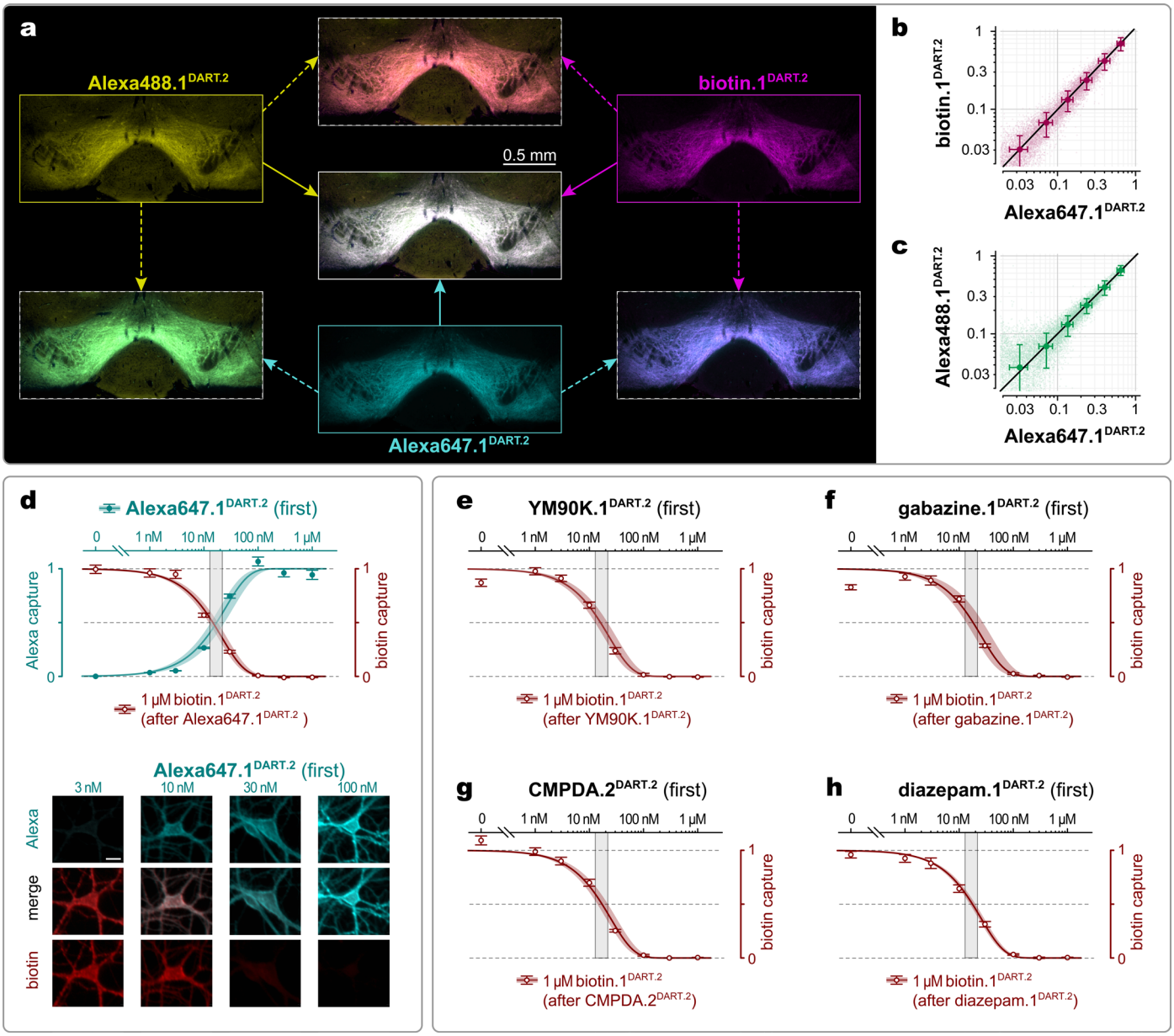

Extended Data Fig. 4 | Diffusion and capture of diverse DART.2 reagents. (a-c) Histological measure of diffusion. A mixture of DART reagents (Alexa488.1$^{DART.2}$, Alexa647.1$^{DART.2}$, and biotin.1$^{DART.2}$) were co-infused into $^{+}HTP_{GPI}$ expressing mice. Images are representative from one mouse. Error bars are binned mean ± SEM, over pixels from two mice. **(d-h) Pulse-chase capture in cultured hippocampal neurons.** A dose-response with Alexa647.1$^{DART.2}$ or various Rx$^{DART.2}$ reagents was initially executed, followed by a chase with biotin.1$^{DART.2}$. Images in panel d show representative raw images (scale bar 10 µm). Each dose-response shows data from 8 coverslips (one per concentration); y-axis shows normalized capture (mean ± 95% CI from all neurons on one coverslip via regression-slope analysis). CC_{50} values are indicated by gray vertical shading.

https://doi.org/10.1038/s41592-024-02292-9

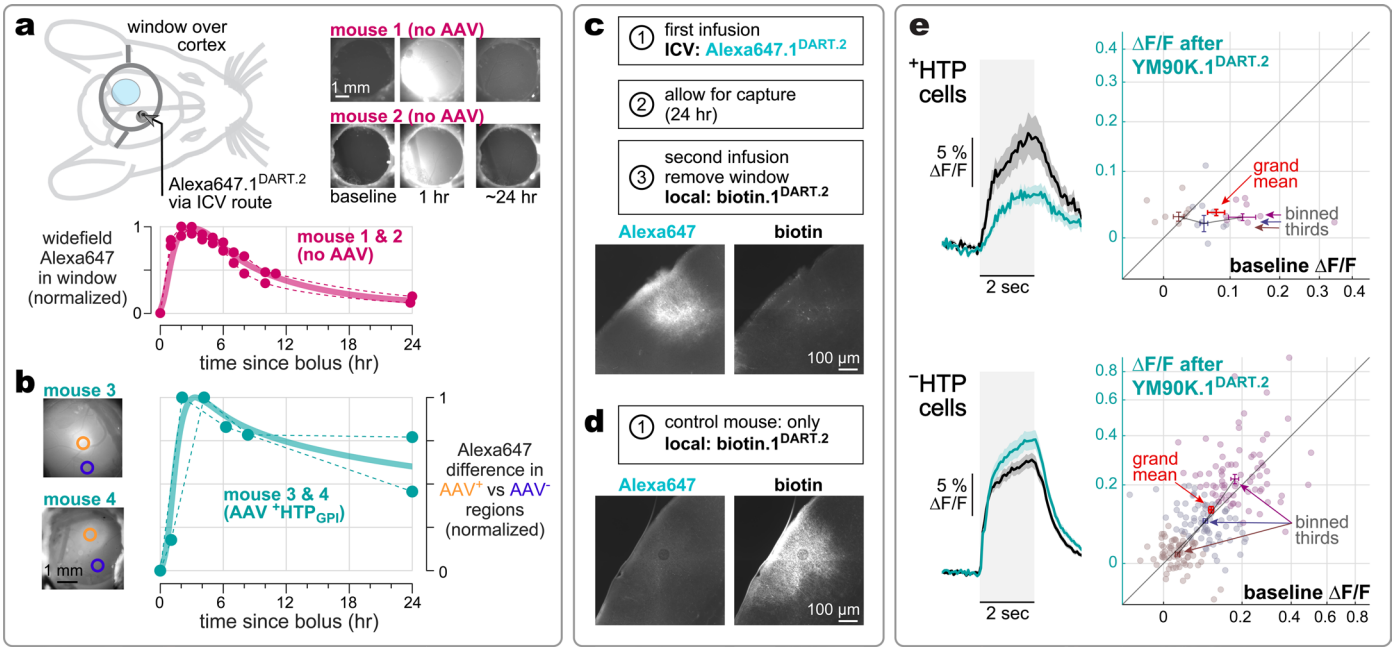

Extended Data Fig. 5 | Lateral ventricle pharmacodynamics. (a) Ambient ICV pharmacokinetics. Two mice, not treated with AAV, received a bolus of Alexa647.1$^{DART.2}$ (2 µL over 20 min) into the contralateral ventricle and were imaged through the cranial window. Fluorescence intensity within a specific region of interest (ROI) was analyzed over time and normalized to its maximum and minimum values. **(b) Tethered ICV pharmacokinetics.** Two SOM::Cre mice with sparse AAV-DIO-$^{+}$HTP$_{GPI}$ expression in the visual cortex received an ICV bolus of 0.3 nmole Alexa647.1$^{DART.2}$ + 3 nmole YM90K.1$^{DART.2}$ (2 µL volume) into the contralateral ventricle. Tethered reagent was estimated via background-subtracted fluorescence (orange virus-expressing region minus blue control region) and was plotted as a function of time since bolus. **(c-d) Pulse-chase experiment.** Injection of biotin.1$^{DART.2}$ directly into the cortex of AAV-DIO-$^{+}$HTP$_{GPI}$ mice. One mouse with (panel c) and one mouse without (panel d) a prior ICV bolus of 0.3 nmole Alexa647.1$^{DART.2}$ + 3 nmole YM90K.1$^{DART.2}$. **(e) Visual-grating experiments.** Traces to the left are reproduced from Fig. 4g. To the right are scatterplots comparing each cell's response before vs after YM90K.1$^{DART.2}$ administration. Each symbol is one cell, with error bars indicating the grand mean ± SEM (red), and the binned mean ± SEM for low-activity (brown), mid-range (blue) and high-activity (purple) subsets.

https://doi.org/10.1038/s41592-024-02292-9

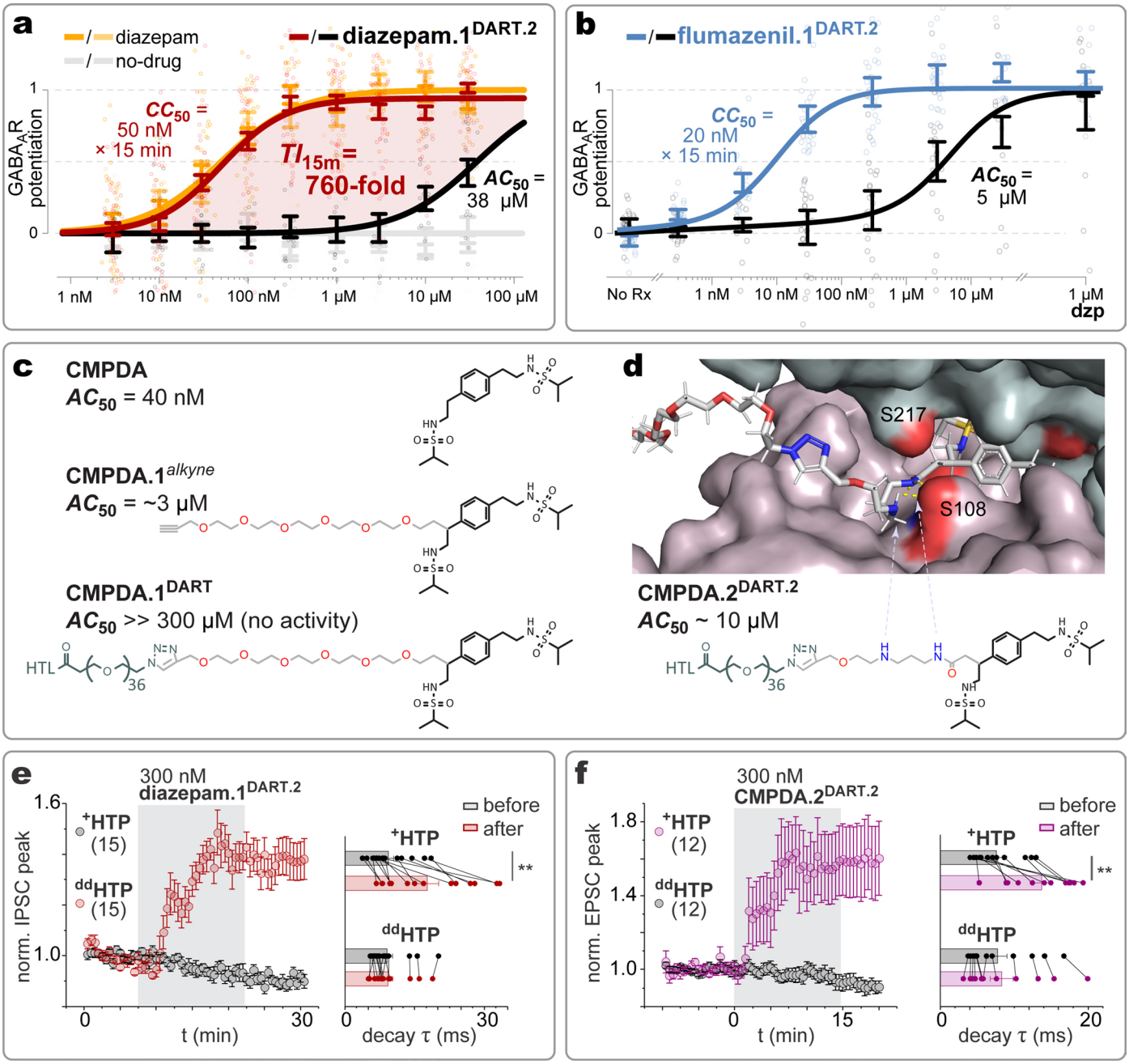

Extended Data Fig. 6 | Design and function of positive allosteric modulators. **(a) $GABA_AR$ PAM assay**. ChR2, GCaMP6s and $^{+}$HTP/^{dd}HTP co-expressed in the same neuron, with excitatory synapses blocked. Low-dose GABA (3 µM) partially activates endogenous $GABA_ARs$ (=0 on vertical axis); maximum allostery calibrated with 1 µM diazepam for each cell (= 1 on vertical axis). Error bars are mean ± SEM over cells. For diazepam.$1^{DART.2}$, CC_{50} = 50 nM × 15 min (red, $^{+}$HTP: n = 40 cells) and AC_{50} = 38,000 nM (black, ^{dd}HTP: n = 14 cells), yielding TI_{15m} = 760-fold. Traditional diazepam (orange; $^{+}$HTP / ^{dd}HTP: n = 17 / 6 cells). Negative control was performed with no drug (gray; $^{+}$HTP / ^{dd}HTP: n = 65 / 24 cells). **(b) Flumazenil.$1^{DART.2}$ is a full-strength PAM**. Assay as in panel a; data is mean ± SEM over cells (blue, $^{+}$HTP: n = 24 cells; black, ^{dd}HTP: n = 24 cells). **(c) CMPDA derivatives**. Structure and AC_{50} of CMPDA, CMPDA.1^{alkyne}, and CMPDA.1^{DART}. **(d) CMPDA spacer model**. Top: design of CMPDA.2 spacer (PDB 3RNN). Electropositive (blue atoms) and predicted hydrogen bonding to S108. Bottom: Structure and AC_{50} of CMPDA.$2^{DART.2}$. **(e) Peak and time-constant analyses for diazepam.$1^{DART.2}$**. Left: IPSC peak (baseline normalized; mean ± SEM over cells) reaches 1.4 ± 0.06 for $^{+}$HTP vs 0.9 ± 0.02 for ^{dd}HTP; p = 1.4×10^{-7} (two-sided unpaired t-test). Right: IPSC time constant (exponential fit of IPSC decay). Baseline-normalized values (after / before ratio; mean ± SEM over cells) are 2.0 ± 0.2 for $^{+}$HTP vs 1.0 ± 0.03 for ^{dd}HTP; p = 2.7×10^{-4} (two-sided unpaired t-test). **(f) Peak and time-constant analyses for CMPDA.$2^{DART.2}$**. Left: EPSC peak (baseline normalized; mean ± SEM over cells) reaches 1.6 ± 0.2 for $^{+}$HTP vs 0.95 ± 0.03 for ^{dd}HTP; p = 0.005 (two-sided unpaired t-test). Right: EPSC time constant (exponential fit of EPSC decay). Baseline-normalized values (after / before ratio; mean ± SEM over cells) are 2.1 ± 0.3 for $^{+}$HTP vs 1.0 ± 0.03 for ^{dd}HTP; p = 0.007 (two-sided unpaired t-test).

nature portfolio

Corresponding author(s): Michael R. Tadross

Last updated by author(s): 4/24/2024

Reporting Summary

Nature Portfolio wishes to improve the reproducibility of the work that we publish. This form provides structure for consistency and transparency in reporting. For further information on Nature Portfolio policies, see our Editorial Policies and the Editorial Policy Checklist.

Statistics

For all statistical analyses, confirm that the following items are present in the figure legend, table legend, main text, or Methods section.

n/a	Confirmed	
☐	☒	The exact sample size (*n*) for each experimental group/condition, given as a discrete number and unit of measurement
☐	☒	A statement on whether measurements were taken from distinct samples or whether the same sample was measured repeatedly
☐	☒	The statistical test(s) used AND whether they are one- or two-sided *Only common tests should be described solely by name; describe more complex techniques in the Methods section.*
☐	☒	A description of all covariates tested
☐	☒	A description of any assumptions or corrections, such as tests of normality and adjustment for multiple comparisons
☐	☒	A full description of the statistical parameters including central tendency (e.g. means) or other basic estimates (e.g. regression coefficient) AND variation (e.g. standard deviation) or associated estimates of uncertainty (e.g. confidence intervals)
☐	☒	For null hypothesis testing, the test statistic (e.g. *F*, *t*, *r*) with confidence intervals, effect sizes, degrees of freedom and *P* value noted *Give P values as exact values whenever suitable.*
☒	☐	For Bayesian analysis, information on the choice of priors and Markov chain Monte Carlo settings
☒	☐	For hierarchical and complex designs, identification of the appropriate level for tests and full reporting of outcomes
☒	☐	Estimates of effect sizes (e.g. Cohen's *d*, Pearson's *r*), indicating how they were calculated

Our web collection on statistics for biologists contains articles on many of the points above.

Software and code

Policy information about availability of computer code

Data collection	All data collection software is described in the methods section of the manuscript. Acquisition software used includes cellSens Dimension (Olympus, ver 4.2), Ethovision (Noldus, ver XT10), Clampfit (Axon Instruments, ver 10.7), and MicroManager (NIH).
Data analysis	All analysis is described in the methods section of the manuscript,. Analysis software used includes MATLAB (MathWorks, Inc., ver 2018a), ImageJ (NIH), Scanbox (Neurolabware), Chemdraw (PerkinElmer, ver 19.1.1.21), Instant JChem (ChemAxon), ACD Spectrus Processor (ACD Labs), and CaImAn (Github). Code that support the findings of this study are available at https://github.com/tadrosslab/DART.2

For manuscripts utilizing custom algorithms or software that are central to the research but not yet described in published literature, software must be made available to editors and reviewers. We strongly encourage code deposition in a community repository (e.g. GitHub). See the Nature Portfolio guidelines for submitting code & software for further information.

Data

Policy information about availability of data

All manuscripts must include a data availability statement. This statement should provide the following information, where applicable:

- Accession codes, unique identifiers, or web links for publicly available datasets
- A description of any restrictions on data availability
- For clinical datasets or third party data, please ensure that the statement adheres to our policy

Source data are provided for electrophysiology experiments at https://github.com/tadrosslab/DART.2. Imaging datasets, due to their large size, are available upon request and will be fulfilled by the corresponding author.

Human research participants

Policy information about studies involving human research participants and Sex and Gender in Research.

Reporting on sex and gender	No human research
Population characteristics	No human research
Recruitment	No human research
Ethics oversight	No human research

Note that full information on the approval of the study protocol must also be provided in the manuscript.

Field-specific reporting

Please select the one below that is the best fit for your research. If you are not sure, read the appropriate sections before making your selection.

☒ Life sciences ☐ Behavioural & social sciences ☐ Ecological, evolutionary & environmental sciences

For a reference copy of the document with all sections, see nature.com/documents/nr-reporting-summary-flat.pdf

Life sciences study design

All studies must disclose on these points even when the disclosure is negative.

Sample size	Detailed in figure legend and methods. No statistical methods were used to predetermine sample size. Resulting sample sizes were decided according to the type of experiment performed (cultured neuronal assays, ex vivo electrophysiology, or animal behavior), informed by past work, to ensure that sample sizes were sufficient for statistical conclusions to be drawn.
Data exclusions	Detailed in methods. No data was excluded. As described in the methods, we obtained quality-control metrics for individual cells (in cultured neuronal assays) and for individual mice (in behavioral work) to quantify the extent of viral expression and/or tracer-DART capture. This allowed individual samples to be binned according to the efficacy of the manipulation.
Replication	Detailed in methods. All attempts at replication over multiple neuronal preparations and multiple mice were successful.
Randomization	Detailed in methods. In cultured neurons, data obtained to compare two or more reagents (e.g., YM90K.1DART.1 vs YM90K.1DART.2) was obtained with experimental groups tested side-by-side, such that all comparison groups were equally represented in each batch of cells. For slice, retina, and mouse behavior, positive vs negative groups (e.g., +HTP vs ddHTP mice) were interleaved and run side-by-side, using cage-mates when possible, and balancing groups to minimize confounding differences (e.g., animal sex, experimenter, time of year), with the goal of isolating the experimental variable of interest.
Blinding	Detailed in methods. Blinding was not included in this study, however all analyses were automated in a manner that prevented experimenter bias and influence on the resulting outcomes.

Reporting for specific materials, systems and methods

We require information from authors about some types of materials, experimental systems and methods used in many studies. Here, indicate whether each material, system or method listed is relevant to your study. If you are not sure if a list item applies to your research, read the appropriate section before selecting a response.

Materials & experimental systems

n/a	Involved in the study
☒	☐ Antibodies
☐	☒ Eukaryotic cell lines
☒	☐ Palaeontology and archaeology
☐	☒ Animals and other organisms
☒	☐ Clinical data
☒	☐ Dual use research of concern

Methods

n/a	Involved in the study
☒	☐ ChIP-seq
☒	☐ Flow cytometry
☒	☐ MRI-based neuroimaging

Eukaryotic cell lines

Policy information about cell lines and Sex and Gender in Research

Cell line source(s)	Cell lines were only used for AAV prep. The cell lines and their authentication was performed by the Duke Viral Vector core and Vector Builder.
Authentication	See above. Authentication was performed by the Duke Viral Vector core and Vector Builder.
Mycoplasma contamination	Duke Viral Vector Core and Vector Builder have verified that cell lines tested negative for mycoplasma contamination.
Commonly misidentified lines (See ICLAC register)	N/A

Animals and other research organisms

Policy information about studies involving animals; ARRIVE guidelines recommended for reporting animal research, and Sex and Gender in Research

Laboratory animals	Detailed in methods. Rats: Sprague-Dawley (mixed multiple males and females used for primary neuronal cultures, postnatal day 0 to 1). Mice: Drd1a-Cre (6 males, 8 females, 10-20 weeks old), DAT-Ires-cre (26 males, 21 females , 8-20weeks old), SST-Cre (2 males, 1 female, P45-60), PV-Cre (22 males, 38 females, 12-24 weeks old), BACα6Cre-AxAi148D (6 males, 4 females, P50-60).
Wild animals	No wild animals were used in this study.
Reporting on sex	Detailed in methods. Relevant details related to sex and gender is provided above. Sex was considered in study design with regards to balanced representation in each of the experiments, and was determined based on vivarium assignment followed by experimenter verification. No sex-based differences were seen.
Field-collected samples	No field collected samples were used in the study.
Ethics oversight	Detailed in methods. All animal experiments were approved by the Duke Institutional Animal Care and Use Committee, an AAALAC accredited program registered with the USDA Public Health Service and the NIH Office of Animal Welfare Assurance, and conform to all relevant regulatory standards (Tadross protocols A160-17-06, A113-20-05, A091-23-04).

Note that full information on the approval of the study protocol must also be provided in the manuscript.